

1           **LSA SAF Meteosat FRP Products: Part 2 - Evaluation and**  
2           **demonstration for use in the Copernicus Atmosphere Monitoring**  
3           **Service (CAMS)**

4  
5  
6   Roberts, G<sup>1\*</sup>., Wooster, M. J<sup>23</sup>., Xu, W<sup>2</sup>., Freeborn, P. H<sup>6</sup>., Morcrette, J-J<sup>5</sup>., Jones, L<sup>5</sup>,  
7   Benedetti, A<sup>5</sup>, Jiangping, H<sup>2</sup>., Fisher, D<sup>2</sup>. and Kaiser, J. W<sup>4</sup>

8  
9   \*corresponding author

10  
11   1) Geography and Environment, University of Southampton, Southampton, UK

12   2) Department of Geography, Kings College London, London, UK

13   3) NERC National Centre for Earth Observation, UK

14   4) Max Planck Institute for Chemistry, Mainz, Germany

15   5) European Center for Medium-Range Weather Forecasts, Reading, UK

16   6) Fire Sciences Laboratory, Missoula, USA

17  
18  
19   **ABSTRACT**

20  
21   Characterising the dynamics of landscape scale wildfires at very high temporal resolutions is  
22   best achieved using observations from Earth Observation (EO) sensors mounted onboard  
23   geostationary satellites. As a result, a number of operational active fire products have been  
24   developed from the data of such sensors. An example of which are the Fire Radiative Power  
25   (FRP) products, the FRP-PIXEL and FRP-GRID products, generated by the Land Surface  
26   Analysis Satellite Applications Facility (LSA SAF) from imagery collected by the Spinning  
27   Enhanced Visible and Infrared Imager (SEVIRI) on-board the Meteosat Second Generation  
28   (MSG) series of geostationary EO satellites. The processing chain developed to deliver these  
29   FRP products detects SEVIRI pixels containing actively burning fires and characterises their  
30   FRP output across four geographic regions covering Europe, part of South America and  
31   northern and southern Africa. The FRP-PIXEL product contains the highest spatial and  
32   temporal resolution FRP dataset, whilst the FRP-GRID product contains a spatio-temporal  
33   summary that includes bias adjustments for cloud cover and the non-detection of low FRP

34 fire pixels. Here we evaluate these two products against active fire data collected by the  
35 Moderate Resolution Imaging Spectroradiometer (MODIS), and compare the results to those  
36 for three alternative active fire products derived from SEVIRI imagery. The FRP-PIXEL  
37 product is shown to detect a substantially greater number of active fire pixels than do  
38 alternative SEVIRI-based products, and comparison to MODIS on a per-fire basis indicates a  
39 strong agreement and low bias in terms of FRP values. However, low FRP fire pixels remain  
40 undetected by SEVIRI, with errors of active fire pixel detection commission and omission  
41 compared to MODIS ranging between 9 - 13% and 65 - 77% respectively in Africa. Higher  
42 errors of omission result in greater underestimation of regional FRP totals relative to those  
43 derived from simultaneously collected MODIS data, ranging from 35% over the Northern  
44 Africa region to 89% over the European region. High errors of active fire omission and FRP  
45 underestimation are found over Europe and South America, and result from SEVIRI's larger  
46 pixel area over these regions. An advantage of using FRP for characterising wildfire  
47 emissions is the ability to do so very frequently and in near real time (NRT). To illustrate the  
48 potential of this approach, wildfire fuel consumption rates derived from the SEVIRI FRP-  
49 PIXEL product are used to characterise smoke emissions of the 2007 'mega fire' event  
50 focused on Peloponnese (Greece) and used within the European Centre for Medium-Range  
51 Weather Forecasting (ECMWF) Integrated Forecasting System (IFS) as a demonstration of  
52 what can be achieved when using geostationary active fire data within the Copernicus  
53 Atmosphere Monitoring Service (CAMS). Qualitative comparison of the modelled smoke  
54 plumes with MODIS optical imagery illustrates that the model captures the temporal and  
55 spatial dynamics of the plume very well, and that high temporal resolution emissions  
56 estimates such as those available from geostationary orbit are important for capturing the sub-  
57 daily variability in smoke plume parameters such as aerosol optical depth (AOD), which are  
58 increasingly less well resolved using daily or coarser temporal resolution emissions datasets.  
59 Quantitative comparison of modelled AOD with coincident MODIS and AERONET AOD  
60 indicates that the former is overestimated by ~20 - 30%, but captures the observed AOD  
61 dynamics with a high degree of fidelity. The case study highlights the potential of using  
62 geostationary FRP data to drive fire emissions estimates for use within atmospheric transport  
63 models such as those implemented in the Monitoring Atmospheric Composition and Climate  
64 (MACC) series of projects for the CAMS.

65  
66  
67

## 68 1. INTRODUCTION

69

### 70 *1.1. Biomass Burning Emissions and Meteosat SEVIRI FRP Products from the LSA SAF*

71

72 Biomass burning emissions databases derived from Earth Observation (EO) satellite data,  
73 such as the widely used Global Fire Emissions Database (GFED; van der Werf *et al.*, 2006;  
74 2010), typically follow the approach proposed by Seiler and Crutzen (1980) and estimate fire  
75 emissions via the multiplication of burned area ( $\text{m}^2$ ), fuel load ( $\text{kg m}^{-2}$ ) and combustion  
76 completeness (unitless, 0-1) estimates. Emissions databases developed in this manner have  
77 been widely applied to deliver wildfire emissions of trace gases and aerosols for use in  
78 atmospheric transport models (Mu *et al.*, 2011; Tsyro *et al.*, 2007). However, whilst excellent  
79 for many applications, some limitations of this ‘burned area’ based approach are that it works  
80 only after the fire event, cannot be applied in near real-time, and has a relatively low temporal  
81 resolution that provides little or no information on the variability of the emissions during the  
82 fire itself. All these maybe limitations when modelling certain aspects of fire emissions  
83 transport and generally preclude use of the approach in real-time atmospheric monitoring or  
84 forecasting systems (Reid *et al.*, 2004). The companion paper to this work, Wooster *et al.*  
85 (2015) describes the geostationary Meteosat SEVIRI Fire Radiative Power (FRP) products  
86 being generated operationally by the EUMETSAT Land Surface Analysis Satellite  
87 Applications Facility (LSA SAF; <http://landsaf.meteo.pt/>). This type of geostationary active  
88 fire product offers an alternative route to biomass burning emissions estimation based on  
89 assessments of the thermal energy being radiated away from fires, and can do so in near real-  
90 time with frequent updates whilst the fires are still burning, though there are also some  
91 limitations caused mainly by fires having too low a fire radiative power remaining  
92 undetectable with the relatively coarse spatial resolution SEVIRI observations (Roberts and  
93 Wooster, 2008). Whilst Wooster *et al.* (2015) describe the methodologies and algorithms  
94 used to produce the LSA SAF Meteosat FRP products, and their information characteristics,  
95 the purpose of the current work is to (i) provide a full evaluation of the product compared to  
96 other real-time active fire products derived from the same SEVIRI observations, (ii) to  
97 provide a product validation via comparisons to the widely used and higher spatial resolution  
98 (albeit lower temporal resolution) MODIS active fire detections, and (iii) to demonstrate how  
99 the product can be used as a high temporal resolution biomass burning emissions driver  
100 within a case study that exploits components of the prototype CAMS  
101 (<http://www.copernicus-atmosphere.eu/>)

102

### 103 ***1.2. Satellite Earth Observation Active Fire Products***

104 Active fire products that are based on detecting the thermal radiation being emitted by  
105 landscape scale fires have been available for over three decades from numerous polar orbiting  
106 and geostationary satellites (Prins *et al.*, 1994; Prins *et al.*, 1998; Matson, 1981, Justice *et al.*,  
107 1998; Giglio, 2003b). In addition to simple detection, Dozier (1981) first demonstrated the  
108 additional potential to estimate a fire's subpixel effective temperature and fractional area, and  
109 this approach has been applied in the Wildfire Automated Biomass Burning Algorithm  
110 (WFABBA) to data from the Geostationary Operational Environmental Satellite (GOES) for  
111 over two decades (Prins *et al.*, 1994). Building on this idea, the FRP route to characterising  
112 active fires and estimate wildfire emissions was first proposed by Kaufman *et al.* (1996). The  
113 FRP approach is based on the understanding that the amount of heat produced by burning a  
114 fixed mass of biomass is relatively invariant to vegetation type (Jenkins *et al.*, 1998). By  
115 measuring the component of this "heat of combustion" that is radiated away from the surface,  
116 the amount of vegetation being burned per second can then be estimated (Wooster *et al.*,  
117 2003; Wooster *et al.*, 2005; Freeborn *et al.*, 2008). An advantage of the FRP approach for  
118 estimating smoke emissions to the atmosphere is that it is based on a direct remotely sensed  
119 observation, and a large number of polar and geostationary satellite instruments have the  
120 requisite midwave infrared (MWIR) waveband required to estimate FRP using the MIR  
121 radiance approach of Wooster *et al.* (2003; 2005). The Moderate Resolution Imaging  
122 Spectroradiometer (MODIS) instruments onboard the Terra and Aqua satellites have been  
123 providing FRP measurements since 2000 and 2002 respectively (Kaufman *et al.*, 1998; Giglio  
124 *et al.*, 2003b) and is currently supported by the Visible Infrared Imaging Radiometer Suite  
125 (VIIRS) onboard Suomi-NPP (Csiszar *et al.*, 2013) and the soon-to-be-launched Sea and  
126 Land Surface Temperature Radiometer (SLSTR) onboard Sentinel-3 (Wooster *et al.*, 2012).  
127 Geostationary instruments, such as the Geostationary Operational Environmental Satellite  
128 (GOES) imager (Xu *et al.*, 2010), are also providing FRP measurements at much higher  
129 temporal resolution but at lower spatial resolution and coverage, and those from the Meteosat  
130 SEVIRI instrument (Wooster *et al.*, 2015) are the target of the current work.

131

### 132 ***1.3. Wildfire Emissions Datasets from FRP Observations***

133 Information on the fuel consumption totals required to build wildfire emissions inventories  
134 have already been developed using FRP data derived from polar-orbiter (Vermote *et al.*,  
135 2009; Ellicott *et al.*, 2009; Kaiser *et al.*, 2012) and geostationary satellite EO data (Pereira *et*

136 *al.*, 2011; Roberts *et al.*, 2011). A limitation associated with the former is their intermittent  
137 observation of the diurnal fire cycle, which needs to be characterised in order to estimate  
138 daily Fire Radiative Energy (FRE; the temporal integration of FRP). MODIS typically  
139 provides around four daily observations depending on latitude which, when accumulated over  
140 a sufficiently long time period, have been exploited to model the diurnal fire cycle and  
141 estimate total emissions over 8-day or longer periods (Vermote *et al.*, 2009; Ellicott *et al.*,  
142 2009). Geostationary FRP datasets provide much higher observation frequencies, and thus  
143 unparalleled data on the diurnal fire cycle (e.g. Roberts and Wooster, 2007; Roberts *et al.*,  
144 2009;), and Zhang *et al.* (2012) illustrate one way such data can be used to develop a near  
145 global biomass burning emissions dataset at hourly type temporal resolutions. However, a  
146 limitation of geostationary data is their coarse spatial resolution, which results biases in  
147 regional-scale FRP and FRE due to the omission of small and/or low intensity wildfires  
148 (Roberts *et al.*, 2005; Xu *et al.*, 2010). Freeborn *et al.* (2009) addressed this issue by  
149 synthesising a ‘virtual’ FRP product via the integration of both geostationary and polar-  
150 orbiter FRP data, maintaining the high temporal resolution of geostationary data whilst  
151 simultaneously adjusting them for the active fire detection biases using the higher spatial  
152 resolution MODIS measurements. Roberts *et al.* (2011) blended geostationary FRP data with  
153 MODIS-derived burned area information to meet a similar objective.

154

155 Perhaps the most obvious advantage FRP-based biomass burning emissions inventories offer  
156 over a burned area based inventory is their near real-time capability, since the thermal  
157 radiation being emitted by the active fires is being sensed whilst the fire is actually burning,  
158 rather than somewhat after the event. As a result, FRP-derived emissions estimates are being  
159 increasingly applied to characterise wildfire emissions for use in near real time atmospheric  
160 transport models. Sofiev *et al.* (2009) use MODIS FRP measurements to characterise  
161 particulate matter (PM) emissions using the method proposed by Ichoku and Kaufmann  
162 (2005), and the dispersion of the resulting emissions are propagated using the System for  
163 Integrated modeLLing of Atmospheric coMposition (SILAM) dispersion model. In this  
164 approach, the diurnal variation of emissions is specified as being 25% greater than the daily  
165 mean during the day, and 25% less than the mean during the night. Kaiser *et al.* (2009a;  
166 2012) developed the Global Fire Assimilation System (GFAS) to prescribe wildfire emissions  
167 for use in the CAMS, potentially calculating the FRP density emitted by actively burning  
168 fires ( $\text{mW m}^{-2}$ ) using a variety of FRP measurements from different spacecraft. However, in  
169 the NRT version of GFAS used currently only FRP measurements from MODIS are used.

170 The FRE density ( $\text{J m}^{-2}$ ) is estimated by temporally integrating the MODIS-derived FRP  
171 density using a Kalman filter. Most recently, Turquety *et al.* (2014) used SEVIRI FRP  
172 measurements from the LSA SAF products to prescribe the fire diurnal cycle for the  
173 APIFLAME European fire emissions model, and Baldassarre *et al.* (2015) used both the LSA  
174 SAF SEVIRI FRP products and other active fire products to simulate the emissions and  
175 emissions transport of a large fire in Turkey.

176

177 This manuscript provides a detailed evaluation of the Meteosat SEVIRI FRP products  
178 available from the LSA SAF, both the full resolution FRP-PIXEL product and the reduced  
179 resolution FRP-GRID product, both available in near real time and in archived form  
180 (<http://landsaf.meteo.pt/>), and provides a detailed example of their use in characterising  
181 wildfire emissions and its atmospheric transport at high temporal resolution. Section 2  
182 provides a brief product summary, and readers are referred to the companion paper (Wooster  
183 *et al.*, 2015) for a more detailed description of the algorithms used to derive the information  
184 from the raw SEVIRI level 1.5 observations. Section 3 describes a detailed inter-comparison  
185 of the LSA SAF SEVIRI FRP-PIXEL product with both the MODIS active fire products  
186 (Giglio *et al.*, 2003), and three alternative active fire products also derived from SEVIRI  
187 observations: namely the WFABBA (Prins *et al.*, 1998), Fire Detection and Monitoring  
188 (FDeM; Amraoui *et al.*, 2010) and Active Fire Monitoring (FIR) product (Joro *et al.*, 2008).  
189 Section 4 evaluates the specific performance of spatio-temporal summary ‘FRP-GRID’  
190 product available from the LSA SAF, which incorporates statistical adjustments for SEVIRI’s  
191 regional FRP biases, whilst Section 5 describes use of the FRP-PIXEL product for  
192 parameterising wildfire emissions at high temporal resolution within the ECMWF Integrated  
193 Forecasting System (IFS) atmospheric chemistry and transport model that is used to deliver  
194 the CAMS (<http://www.copernicus-atmosphere.eu/>).

195

## 196 **2. METEOSAT SEVIRI FRP PRODUCTS FROM THE EUMETSAT LSA SAF**

197

198 The Spinning Enhanced Visible and Infrared Imager (SEVIRI) onboard the Meteosat Second  
199 Generation (MSG) series of satellites acquires observations every 15 minutes over the Earth’s  
200 disk centred on West Africa, including in MWIR and long-wave infrared (LWIR) wavebands.  
201 Data collected in these wavebands enables the detection of active fires using the type of  
202 algorithms detailed in Li *et al.* (2001), and this has been exploited for the development of a  
203 number of geostationary active fire products based on SEVIRI observations. One of these is

204 the Meteosat SEVIRI FRP-PIXEL family of products that has been produced operationally  
205 since 2008 by the European Organisation for the Exploitation of Meteorological Satellites  
206 (EUMETSAT) LSA SAF (<http://landsaf.meteo.pt>). The LSA SAF Meteosat SEVIRI FRP  
207 product suite currently contains two components; (i) the FRP-PIXEL product which records  
208 active fire information at the full temporal and spatial resolution of SEVIRI, and (ii) the FRP-  
209 GRID product that provides a spatio-temporal summary of the FRP-PIXEL product, along  
210 with statistical adjustments for cloud cover and for the regional biases caused by the lowest  
211 FRP fires being undetectable with SEVIRI.

212

### 213 **2.1 FRP-PIXEL Product Summary**

214

215 The Level 2 FRP-PIXEL product provides information on the spatial location, thermal  
216 properties, atmospherically corrected FRP and uncertainty of pixels containing actively  
217 burning fires every 15 minutes over Europe, North and South Africa and part of South  
218 America (Figure 1), based upon an extended version of the geostationary Fire Thermal  
219 Anomaly (FTA) active fire detection algorithm of Roberts and Wooster (2008) and a set of  
220 FRP estimation routines that are together fully detailed in Wooster *et al.* (2015). The structure  
221 of the FRP-PIXEL product is also detailed in Wooster *et al.* (2015), and follows the heritage  
222 of the MODIS active fire products (Giglio *et al.*, 2003) but separated into two discrete files,  
223 (i) the FRP-PIXEL ‘Quality Product’ file, a 2D dataset that provides information on the status  
224 of each SEVIRI pixel in the geographic region under study (e.g. whether it is a cloud, water,  
225 or land pixel, whether it has been classed as containing an active fire etc; Wooster *et al.*,  
226 2015), and (ii) a smaller ‘List Product’ file that provides detailed information of pixels in  
227 which active fires have been detected (e.g. including the pixel MWIR and LWIR brightness  
228 temperatures, FRP, FRP uncertainty, latitude and longitude, and some of the metrics derived  
229 during algorithm application such as background window size and estimated MWIR band  
230 atmospheric transmissivity).

231

### 232 **2.2 FRP-GRID Product Summary**

233 The Level 3 FRP-GRID product is a spatio-temporal summary of a series of FRP-PIXEL  
234 products. At the regional scale, the FRP-PIXEL product provides a minimum estimate of the  
235 FRP being emitted from landscape fires due to (i) the inability of SEVIRI to detect the lowest  
236 FRP active fire pixels (Roberts and Wooster, 2008; Freeborn *et al.*, 2014a) and (ii) the fact

237 that the assessment of the highest FRP fires suffer from some effects of pixel saturation and  
238 other SEVIRI-specific observation characteristics (Wooster *et al.*, 2015). In order to try  
239 mitigate these impacts on regional FRP estimation, the LSA SAF processing chain generates  
240 the Level 3 FRP-GRID product by temporally accumulating active fire pixels and associated  
241 information from the maximum of four FRP-PIXEL products obtained each hour, grids this  
242 information within 5.0° grid cells, and applies a set of regional bias adjustment factors.  
243 Wooster *et al.* (2015) describe the procedures in full, and an evaluation of the resulting  
244 product performance is presented in Section 4 herein.

245

### 246 **3. FRP-PIXEL PRODUCT PERFORMANCE EVALUATION**

247

248 Here we validate the SEVIRI FRP products using MODIS active fire data. The relatively  
249 high spatial resolution of MODIS' active fire observations (1 km at nadir), and the high  
250 saturation temperature of its MWIR channel (~ 500 K), coupled with its better than daily  
251 availability from two platforms (the Terra and Aqua satellites), ensure that the MODIS active  
252 fire product (Kaufman *et al.*, 1998; Giglio *et al.* 2003) is the standard against which  
253 geostationary active fire products are compared when performing product evaluations (Xu *et*  
254 *al.*, 2010; Schroeder *et al.*, 2014; Roberts and Wooster, 2014). Here we use near-  
255 simultaneously recorded Collection 5 MODIS active fire detections (MOD14 from Terra and  
256 MYD14 from Aqua) as the basis of our LSA SAF SEVIRI FRP Product performance  
257 evaluations. For completeness, we also include a series of other SEVIRI active fire products,  
258 derived using different algorithms and methods to the LSA SAF FRP products, within the  
259 same comparison.

260

#### 261 **3.1 SEVIRI FRP-PIXEL and MODIS Active Fire Product Intercomparison**

262

##### 263 ***3.1.1 Methodology***

264

265 The FRP-PIXEL product is generated in separate files for the four LSA SAF geographic  
266 regions whose boundaries as shown in Figure 1 (Wooster *et al.*, 2015). We conducted the  
267 FRP-PIXEL product performance evaluation using one week of operational FRP-PIXEL data  
268 collected by Meteosat-9 in each of the LSA SAF regions, together with the matching MODIS  
269 MOD14 and MYD14 products. The FRP-PIXEL products of each region were derived from

270 672 separate SEVIRI imaging slots taken every 15 minutes over a 168 hour period in 2008,  
271 with the timing of the products for each geographic region being that corresponding to its  
272 peak fire period; December in Northern hemisphere Africa, and August in the remaining  
273 three regions. Freeborn *et al.* (2014a) previously performed an evaluation of the FRP-  
274 PIXEL product over the Central African Republic (CAR), finding that the products active fire  
275 detection errors of commission reduced greatly (from 24% to 9%) when the MODIS active  
276 fire detections being used as the independent data source were limited to a  $\pm 18.6^\circ$  scan angle.  
277 This is due to the increasing pixel area of MODIS with increasing scan angle, which results  
278 in MODIS itself showing progressively greater active fire errors of omission towards the scan  
279 edge (Freeborn *et al.*, 2011). When comparing large-scan angle MODIS data to active fire  
280 detections made from SEVIRI, it may well be that MODIS actually misses fires that the  
281 SEVIRI FRP-PIXEL product actually correctly detects, but in the absence of any other  
282 information a SEVIRI-to-MODIS performance evaluation would record this as a SEVIRI  
283 commission error. Therefore, to mitigate against the impact of MODIS' decreasing ability to  
284 detect low FRP pixels as MODIS scan angle increases, yet balance this with the need to  
285 maintain sufficient data in our intercomparison, MODIS observations are limited to those  
286 within  $\pm 30^\circ$  scan angle within which MODIS' pixel area increases up to a maximum of 1.7  
287 km<sup>2</sup> from the nadir 1 km<sup>2</sup> size (Freeborn *et al.*, 2011). For each LSA SAF geographic region  
288 we compared the active fire detections made by MODIS within this scan angle limit to the  
289 active fire pixels present in the FRP-PIXEL product subsets covering the same area and  
290 collected at the closest matching time (generally this will be within  $\sim 6$  minutes of the  
291 MODIS overpass). To deal with the differing MODIS and SEVIRI pixel sizes, we remapped  
292 the MODIS active fire data to SEVIRI's imaging grid. SEVIRI's per-pixel point spread  
293 function (PSF) at the sub-satellite point extends more than 5 km radially from the pixel centre  
294 (Wooster *et al.*, 2015), so following the approach of Freeborn *et al.* (2014a) we evaluated  
295 active fire detection performance using the presence of an active fire pixel within a  $3 \times 3$   
296 pixel window centred on the active fire pixel under investigation within this grid as a  
297 matched detection. For SEVIRI errors of commission we searched for the presence of a  
298 matching MODIS pixel for each SEVIRI active fire pixel studied, whilst the reverse analysis  
299 was conducted for SEVIRI errors of omission.

300

301 When undertaking the SEVIRI-to-MODIS FRP intercomparison, this was conducted on a 'per  
302 fire' basis by clustering the MODIS and SEVIRI per-pixel FRP measurements for the same  
303 fire into 'fire pixel clusters' on the basis of spatial closeness (e.g. Zhukov *et al.*, 2006;

304 Roberts and Wooster; 2008; Xu *et al.*, 2011). The MODIS FRP measurements were derived  
305 using the same MIR radiance approach to FRP derivation as is used for SEVIRI (Wooster *et*  
306 *al.*, 2005; 2015), and as will be employed in the forthcoming Collection 6 MODIS Active fire  
307 products (L. Giglio, *pers comm.*). We atmospherically corrected these MODIS FRP estimates  
308 using the same procedure applied when generating the FRP-PIXEL product, detailed in  
309 Wooster *et al.* (2015), based on an atmospheric transmission look-up-table (LUT) developed  
310 using the MODTRAN5 and RTMOM atmospheric radiative transfer models (Berk *et al.*  
311 2005; Govaerts, 2006) and ECMWF forecasts of total water column vapour (interpolated  
312 from an original spatial and temporal resolution of 0.5° and 3 hours). Generally, the  
313 adjustment for the MWIR atmospheric transmission made to the SEVIRI FRP data was larger  
314 than that for MODIS, because the SEVIRI MWIR spectral band used in FRP derivation is  
315 significantly wider than that of MODIS and extends into spectral regions having much lower  
316 atmospheric transmission (Wooster *et al.*, 2015).

317

### 318 **3.1.2 Results**

319 The results of our SEVIRI-to-MODIS per-fire active fire detection intercomparison are  
320 detailed in Table 1, Columns 3 and 4. Taking the north African (NAfr) LSA SAF region as  
321 the first example, this is closest region to the Meteosat sub-satellite point and therefore offers  
322 the highest degree of SEVIRI spatial detail and smallest pixel area. We find that 65% of  
323 MODIS' active fire detections made within this region had no corresponding SEVIRI-  
324 detected active fire within the closest matching (in time) FRP-PIXEL product file. This  
325 'active fire error of omission' rate is higher than the 54% found previously by Roberts and  
326 Wooster (2008) over the same geographic area, but using the prototype SEVIRI FTA  
327 algorithm, a different period satellite (Meteosat-8) and different time period. The reverse  
328 analysis showed that 9% of the Meteosat-9 FRP-PIXEL product active fire pixels had no  
329 matching MODIS active fire pixel, a very similar commission error to that found by Roberts  
330 and Wooster (2008) for the prototype SEVIRI FTA algorithm over the same North African  
331 region.

332

333 SEVIRI FRP-PIXEL product active fire detection performance metrics for the other three  
334 LSA SAF geographic regions are also shown in Table 1, and indicate a substantially  
335 increased active fire omission error in South America and Europe compared to the two  
336 African regions. This is in part due to SEVIRI's increased pixel area and greater view zenith  
337 angle (and thus greater atmospheric attenuation) over the former two regions which are

338 further from the Meteosat sub-satellite point (SSP). South America and Europe have a mean  
339 view zenith angle of 59° and 54° respectively and this significantly raises the minimum per-  
340 pixel FRP detection limit in these areas (Figure 1), meaning a greater proportion of lower  
341 FRP landscape-scale fires fail to be detected by SEVIRI in comparison to the African  
342 regions.

343

344 Figure 2 and Table 1 (Column 5) present the results of the SEVIRI-to-MODIS per-fire FRP  
345 intercomparison. Again taking north Africa as an example, on a per-fire basis there is a strong  
346 correlation between the FRP measures made by SEVIRI in this region and by MODIS  
347 (Figure 2; top left) with over half (53%) of the SEVIRI-to-MODIS matchups having an FRP  
348 difference less than 20%. In fact, a strong level of agreement exists for all regions in terms of  
349 a low FRP bias between the two datasets, but there is significant scatter. Overall, we find that  
350 57% of the FRP-PIXEL products per-fire FRP measures are within 20% of those of MODIS,  
351 and this level of agreement remains consistent even when limiting the comparison to fires  
352 with FRP > 50 MW to ensure we focus on the FRP range where SEVIRI does not clearly  
353 underdetect active fires (e.g. Wooster *et al.*, 2015). This suggests that the degree of variability  
354 seen between the near-simultaneous measures of per-fire FRP provided by SEVIRI and  
355 MODIS is not driven only by active fire pixel errors of omission (e.g. by SEVIRI failing to  
356 detect some of the low FRP fire pixels making up a fire cluster), but maybe impacted by other  
357 aspects of the FRP measurement process coming from:

358 i) uncertainty in the ambient background signal used to calculate the FRP for each  
359 fire pixel with SEVIRI and MODIS data (Wooster *et al.*, 2003; 2005; Zhukov *et al.*,  
360 *et al.*, 2006; Wooster *et al.*, 2015);

361 ii) the  $\pm 6$  minute time difference between corresponding MODIS and SEVIRI  
362 observations of the same fire, during which changes in the active fire  
363 characteristics that determine the fires FRP may occur;

364 iii) the uncertainties present in the MODIS FRP measures coming from the sub-pixel  
365 location of the fire with respect to the sensor instantaneous field of view, recently  
366 been characterised by Freeborn *et al.* (2014c), and with SEVIRI also from certain  
367 image processing operations conducted during the production of SEVIRI level 1.5  
368 data (Wooster *et al.*, 2015).

369 iv) effects of sensor saturation of SEVIRI's MWIR channel at high FRP fire pixels.

370

371 To place the magnitude of the scatter seen in Figure 2 between the SEVIRI FRP-PIXEL  
372 product's FRP measures and those from the MODIS MOD14 and MYD14 products into  
373 context, during the recent Freeborn *et al.* (2014c) study, multiple MODIS FRP measurements  
374 of the same fires made almost simultaneously ( $\ll 1$  sec difference) in consecutive MODIS  
375 scans were compared and some large scan-to-scan differences found. An approximately  
376 normally distributed percentage difference between the two FRP measures, with a mean close  
377 to zero but a standard deviation of 26.6% was determined from a large dataset of such  
378 matchups (Freeborn *et al.*; 2014c). Further investigation showed that the scan-to-scan  
379 differences were largely controlled by the differing sub-pixel location of the fire within the  
380 different MODIS scans, a subject previously indicated as potentially significant with regard  
381 to FRP observations made by the BIRD Hot Spot Recognition Sensor (HSRS; Zhukov *et al.*,  
382 2006). Freeborn *et al.* (2014c) also showed that the scatter reduced as fire clusters containing  
383 increasing numbers of active fire pixels were compared, since the sub-pixel location effects  
384 would increasingly cancel out as more pixels were included in the instantaneous scan-to-scan  
385 FRP inter-comparison. Nevertheless, given the degree of scatter found between even almost  
386 totally simultaneous MODIS FRP observations of the same fire made at the same scan angle  
387 and pixel area by Freeborn *et al.* (2014c), it is unsurprising that higher levels of scatter arises  
388 when comparing FRP data from different sensors (Figure 2; Table 1), where pixel areas, scan  
389 angles and imaging time differences are all somewhat greater. Nevertheless, our results  
390 indicate that when the FRP-PIXEL product and the MODIS active fire products both detect  
391 the same fire, the FRP reported by the two products show small biases. Over the four LSA  
392 SAF regions, 391 individual active fire 'clusters' detected by MODIS and SEVIRI were  
393 compared and 76% (298 fire clusters) had an FRP within 30% of that measured by MODIS.  
394 Given the uncertainties on per-fire FRP retrievals, the LSA SAF target accuracy of the FRP-  
395 PIXEL product is specified as, on a per-fire basis, 70% of the SEVIRI-retrieved FRP values  
396 being within 50% of those simultaneously measured by MODIS. Therefore, the FRP-PIXEL  
397 product significantly exceeds this specification, and actually approaches that specified by the  
398 LSA SAF 'optimal accuracy' definition (70% of retrieved SEVIRI-retrieved FRP value being  
399 within 20% of the MODIS-derived value on a per-fire basis).

400

401 Whilst our per-fire FRP inter-comparison has indicated a comparatively low degree of FRP  
402 bias between the FRP-PIXEL and MODIS MOD14/MYD14 FRP records of the same  
403 successfully detected active fires, there remains a significant degree of regional-scale FRP

404 underestimation by the FRP-PIXEL product due to the inability of the coarser SEVIRI  
405 observations to detect the lowest FRP component of a regions fire regime (Roberts and  
406 Wooster, 2008). Therefore when data from both the MOD14/MYD14 and near-simultaneous  
407 matching FRP-PIXEL products covering the same area (i.e. the area covered by MODIS  
408 within a  $\pm 30^\circ$  scan angle) are compared, SEVIRI reports a lower cumulative ‘regional’ FRP  
409 than does MODIS (Table 1, Column 6). This effect is directly related to SEVIRI’s  
410 aforementioned active fire errors of omission, an effect that is magnified in geographic  
411 regions in which SEVIRI mostly observes at higher view zenith angles. Figure 3 again uses  
412 the example of the North African region, where the slope of the linear of best fit to the  
413 regional FRP totals recorded near simultaneously in the FRP-PIXEL product and the MODIS  
414 active fire products is 0.65. This indicates the relatively small, but certainly not insignificant,  
415 impact of the FRP-PIXEL products active fire errors of omission in this region, which is that  
416 closest to the Meteosat sub-satellite point (SSP) and thus in which the FRP-PIXEL products  
417 active fire errors of omission are lowest (Table 1). Regional FRP underestimation increases  
418 away from the SSP, and appears particularly extreme in the European LSA SAF geographic  
419 region in our inter-comparison. This is in part a result of a large proportion of active fires  
420 being present in Eastern Europe during our inter-comparison period, where the SEVIRI view  
421 zenith angle exceeds  $60^\circ$ . With respect to regional FRP characterisation, the performance of  
422 the FRP-PIXEL product for southern European fires, which lie relatively close to the  
423 Meteosat SSP, is likely to be much closer to that of the North African geographic region.  
424 Section 5 includes study of the August 2007 Greek Fires as a case study example of fires in  
425 this region.

426

### 427 **3.2 Inter-comparison of Alternative SEVIRI Active Fire Products**

428 Since the launch of Meteosat Second Generation in 2002, a number of studies have used  
429 different algorithms to study active fires with SEVIRI observations (e.g. Calle *et al.*, 2009;  
430 Amraoui *et al.*, 2010). This has led to certain other routinely generated SEVIRI active fire  
431 products being available, in addition to the LSA SAF FRP-PIXEL product focused upon  
432 herein. These alternative SEVIRI-based products include the Wildfire Automated Biomass  
433 Burning Algorithm (WFABBA, version 6.5) product (based on the WFABBA fire detection  
434 algorithm of Prins *et al.*, 1998), the Fire Detection and Monitoring (FDeM) product (Amraoui  
435 *et al.*, 2010), and the Active Fire Monitoring (FIR) product (Joro *et al.*, 2008), each of which  
436 essentially generate active fire pixel detections from SEVIRI level 1.5 data as does the FTA  
437 algorithm used within the FRP-PIXEL product processing chain (Wooster *et al.*, 2015).

438

### 439 **3.2.1 Methodology**

440 We assessed the active fire detection performance of the FRP-PIXEL product in comparison  
441 to the three main alternative SEVIRI active fire products, and to the MODIS  
442 MOD14/MYD14 active fire products using the SEVIRI-to-MODIS intercomparison  
443 methodology detailed in Section 3.1. The inter-comparison was conducted using all available  
444 FRP-PIXEL products collected over the southern African LSA SAF geographic region in  
445 August 2014 (a total of 2959), a month when fires are highly prevalent in southern Africa.  
446 For comparison we collected all the available files from the alternative SEVIRI active fire  
447 data products, a total of 2949 for WFABBA (Prins *et al.*, 1998), 2963 for FDeM product  
448 (Amraoui *et al.*, 2010), and 2914 for FIR (Joro *et al.*, 2008). Due to various data collection  
449 and processing issues, not all products were available for all SEVIRI source scenes, as is  
450 evident from the slightly different (max 1.5%) number of products in each case. Also, each  
451 product has different classes of output, and the FIR product for example classifies fire pixels  
452 as either active fires or potential active fires. In this comparison we focus on only confirmed  
453 active fire detections. Similarly, the WFABBA product 'filters' active fire pixels detected only  
454 once in a 24 hour period and classes them less likely to be fires, aiming to reduce the number  
455 of false alarms detected and minimise effects due to sunglint. In our analysis of the  
456 WFABBA active fire product we therefore include four variations of the WFABBA dataset.  
457 These are the inclusion of all fire detections, all the WFABBA 'filtered' detections (where  
458 pixels only detected once during 24 hrs are removed) and the WFABBA 'filtered' detections  
459 keeping only 1) the high probability fires (WFABBA flags 0 to 3) and 2) high and medium  
460 probability fires (WFABBA flags 0 to 4).

461

462 For comparison to the SEVIRI-derived active fire products we used 544 Collection 5 MODIS  
463 MOD14/MYD14 active fire products, acquired over southern hemisphere Africa. To facilitate  
464 comparison with the SEVIRI products, we subset the SEVIRI products to cover the same area  
465 as the MODIS products and selected the set of temporally coincident MODIS active fire  
466 pixels that matched with SEVIRI active fire products in time ( $\pm 6$  minutes). The MODIS  
467 active fire pixels were remapped to SEVIRI's imaging grid and had their FRP  
468 atmospherically corrected using the same approach as detailed in Section 3.1 to match the  
469 methodology used to generate the FRP values within the FRP-PIXEL product. SEVIRI's per-  
470 pixel point spread function (PSF) at the sub-satellite point extends more than 5 km radially  
471 from the pixel centre (Wooster *et al.*, 2015), so following the approach of Freeborn *et al.*

472 (2014a) we evaluated the SEVIRI-derived active fire detection performances against the  
473 presence of MODIS active fire pixels within a  $3 \times 3$  pixel window centred on the SEVIRI  
474 active fire pixel under investigation. Again, as with Section 3.1 the comparison was restricted  
475 to MODIS active fire detections made within a  $\pm 30^\circ$  scan angle (Freeborn *et al.*, 2014a).

476

### 477 **3.2.2 Results**

478

479 The MOD14/MYD14 products contained 286,000 active fire detections during August 2014  
480 over the southern African LSA SAF geographic region, and once remapped onto the SEVIRI  
481 imaging grid, this equated to 112,576 pixels. Within the specified  $\pm 6$  minute MODIS to  
482 SEVIRI imaging time limit, the FRP-PIXEL product detects 33,414 active fire pixels and  
483 29,037 of these are also detected by the remapped MOD14/MYD14 data. This corresponds to  
484 a SEVIRI active fire pixel detection commission error of 13%. Using the same SEVIRI level  
485 1.5 data, the WFABBA, FDeM and FIR active fire products detect 13,008, 7664 and 7151  
486 active fire pixels respectively, and of these, 12,284, 7260 and 6730 are coincident with a  
487 MODIS active fire detection respectively. Hence, the active fire pixel errors of commission  
488 are 5.5%, 5.2% and 5.8% respectively for these three SEVIRI-derived products, active fire  
489 errors of commission rates around half those of the FRP-PIXEL product. The WFABBA  
490 filtered dataset also stratifies active fire detections according to their detection confidence.  
491 We analysed the fire detection performance of the WFABBA filtered dataset by just  
492 including medium and high probability fires (flags 0-4) and only high probability fires (flags  
493 0-3). These filtered WFABBA datasets detect 9736 (flags 0-4) and 8832 (flags 0-3) active  
494 fires and of which 9369 and 8496 are coincident with MODIS active fire pixels. This equates  
495 to a reduced commission rate of 4 % for both whilst the omission rate increases to 87% and  
496 88% respectively.

497

498 A summary of the SEVIRI active fire product intercomparison results is given in Table 2.  
499 The ~13% active fire error of commission rate for the FRP-PIXEL product found here and by  
500 Freeborn *et al.* (2014a) is higher than the ~8% found by Roberts and Wooster (2008, 2014)  
501 using the FTA algorithm prototype. The disparity is in part due to the differing way in which  
502 the operational FTA algorithm applies a high-pass spatial filter to screen out certain false  
503 alarms from the potential fire pixel set (Roberts and Wooster, 2008). As discussed in the  
504 companion paper that describes the fire thermal anomaly (FTA) algorithm in detail (Wooster  
505 *et al.*, 2015), the current LSA SAF implementation of the FTA algorithm (whose

506 performance results are reported in Table 2) has some characteristics that are open to being  
507 updated, namely whether dynamic or static thresholds are used in the spatial filter applied at  
508 the end of the potential fire pixel (PFP) stage, and whether application of the cloud-edge  
509 mask is really necessary (see Wooster *et al.*, 2015 for details). We have tested these  
510 adaptations using one month of data (July, 2015) collected over the same Southern African  
511 region used to perform the evaluation reported in Table 2, and have compared the results to  
512 those from contemporaneous MODIS overpasses. Results show that with both adaptations  
513 applied, the error of commission of the adjusted FTA algorithm compared to MODIS reduce  
514 from the current 14% to 12%, whilst the error of omission remains at 70%. These two  
515 adaptations are therefore now being implemented in the operational FTA processing chain.

516  
517 The minimum FRP detection limit of an active fire detection algorithm is directly  
518 proportional to the pixel area (Roberts and Wooster, 2008; Wooster *et al.*, 2015). If the active  
519 fire detection algorithm of Giglio *et al.* (2003) used to generate the Collection 5  
520 MOD14/MYD14 MODIS active fire products were applied to SEVIRI level 1.5 imagery, the  
521 minimum FRP detection limit at the Meteosat SSP would be 70 - 80 MW, around 10× the  
522 minimum FRP detection limit of the MOD14/MYD14 active fire products due to SEVIRI's ~  
523 10× larger nadir view pixel area. By contrast, the design of the FRP-PIXEL product attempts  
524 to lower the minimum FRP detection limit significantly below this by detecting active fire  
525 pixels whose radiometric signals in the MWIR, LWIR and MWIR-LWIR are raised even  
526 quite minimally above that of the ambient background (Roberts and Wooster, 2008). By  
527 exploiting a variety of spectral and spatial thresholds and contextual processing methods, the  
528 FTA algorithm is sometimes capable of detecting SEVIRI active fire pixels having an FRP  
529 down to ~ 20 MW at the Meteosat SSP. Nevertheless, statistics show that for active fire  
530 pixels below ~ 50 MW the active fire pixel count is underestimated more by SEVIRI  
531 compared to the performance above this threshold (Freeborn *et al.*, 2009). However, by  
532 restricting our comparison of the FRP-PIXEL product to active fire pixels having FRP ≥ 50  
533 MW the active fire pixel error of commission of the FRP-PIXEL product fell only slightly to  
534 12%, indicating that false alarms are not necessarily dominated by these low FRP fire pixels.

535  
536 Whilst our analysis has shown somewhat higher active fire errors of commission for the FRP-  
537 PIXEL product compared to the WFABBA, FIR and FDeM products, we find the latter have  
538 much higher active fire errors of omission. Figure 4 illustrates the variation seen in active fire  
539 pixel detection performance between the different SEVIRI products for one imaging slot (21<sup>st</sup>

540 August, 2014, 13:15 UTC). In this example, the FRP-PIXEL, WFABBA, FDeM and FIR  
541 products detect 1249, 686, 346 and 312 active fire pixels respectively, illustrating a  
542 substantial degree of difference. Furthermore, the fire diurnal cycle retrieved using the four  
543 products from a single day of data shown in Figure 5 highlights the fact that these differences  
544 are maintained over the course of the day, leading to very large variations in the total count of  
545 active fires detected on a daily basis.

546  
547 When compared to the matching MODIS active fire pixel detections, the WFABBA, FDeM  
548 and FIR products contain active fire pixel detections that match 16%, 8% and 5%  
549 respectively of the MODIS active fire pixels, whereas the figure for the LSA SAF FRP-  
550 PIXEL product is substantially higher at 23%. Georgiev and Stoyanova (2013) previously  
551 undertook a limited study of the FRP-PIXEL product performance in south-east Europe, and  
552 determined that it provided a marginally higher active fire detection efficiency than did the  
553 FIR product. Using a wider area of a region with many more fires covering a wide FRP range  
554 we find much larger differences, and indeed the FIR product appears to provide the worst  
555 performance of all the four SEVIRI products in terms of its ability to detect active fire pixels.  
556 Restricting the FRP-PIXEL active fire detections to those pixels  $\geq 50$  MW, the FRP-PIXEL  
557 product still detects 9896, 14864, 15896 more active fire pixels that are coincident with  
558 MODIS than do the WFABBA, FDeM and FIR products respectively. This corresponds to  
559 active fire pixel count differences in excess of  $\sim 175\%$ , even when limiting the detection  
560 regime to an FRP range where all the SEVIRI-derived products should in theory be able to  
561 show a reasonably strong performance.

562  
563 Our analysis of the operational FTA algorithm's performance has shown an active fire pixel  
564 error of omission rate of 77% when comparing the FRP-PIXEL product to simultaneously  
565 collected MODIS active fire pixels. This omission error is similar to that previously found by  
566 Roberts and Wooster (2014) and Freeborn *et al.* (2014a) for the FTA algorithm, and primarily  
567 results from the  $\sim 10\times$  larger nadir pixel area of SEVIRI than MODIS. In comparison, the  
568 errors of omission for the WFABBA, FDeM and FIR products are significantly greater, at  
569 84%, 92% and 95% respectively. Restricting the comparison to those FRP-PIXEL product  
570 pixels having a SEVIRI-retrieved FRP  $\geq 50$  MW, which SEVIRI-based algorithms should be  
571 able to detect quite readily, reduces the FRP-PIXEL product active fire pixel error of  
572 omission to  $\sim 50\%$  in comparison to MODIS.

573

574 In terms of FRP measurements, the ratio between the total cumulative FRP measured within  
575 the same southern African geographic region covered by the near-simultaneous FRP-PIXEL  
576 and MODIS active fire products is 0.48. This represents a lower underestimate of FRP than  
577 might be expected from the FRP-PIXEL omission error rate, and the reason is that the  
578 unidentified active fire pixels are predominantly those having low FRP values ( $\ll 50$  MW).  
579 Restricting the analysis to only those active fires that are correctly identified by both products  
580 provides a cumulative FRP ratio of 0.96, showing an excellent agreement in the regional FRP  
581 assessment when only active fires successfully detected by both sensors are taken into  
582 account. This agrees with the strong-performance in terms of per-pixel FRP assessment seen  
583 in Section 3.1.

584

585 Certain previous studies evaluating the FTA algorithm or prototype FRP-PIXEL datasets  
586 (e.g. Roberts and Wooster, 2008; Xu *et al.*, 2010; Roberts *et al.*, 2014) have applied an  
587 alternative approach when comparing these to MODIS active fire datasets. Rather than the  
588 per-pixel approach to inter-comparison applied above, Freeborn *et al.* (2014a) grouped active  
589 fire pixels into contiguous clusters based on their spatial closeness to other active fire pixels  
590 in the same manner as that described in Section 3.1 for the per-fire FRP intercomparison. To  
591 strengthen the link between this work and these previous findings, active fire pixels within  
592 each of the active fire products tested were also clustered into spatially contiguous groupings,  
593 and the active fire detection errors of commission and omission calculated based on a ‘fire  
594 cluster’ basis instead of for the individual fire pixels. We used a similar strategy for this inter-  
595 comparison as used at the pixel scale, specifically searching the surrounding  $3 \times 3$  pixels for  
596 matching active fires in the products to be compared. Using this ‘clustering’ approach, we  
597 found the error rates of the FRP-PIXEL product to be higher than those determined using the  
598 per-pixel approach, with errors of commission and omission of 19% and 85% respectively  
599 when compared to the matching MOD14/MYD14 products. Again, if only those fire clusters  
600 having an  $\text{FRP} \geq 50$  MW are included, these reduce to 18% and 57% respectively,  
601 demonstrating in particular a high success of active fire detection in this region of the FRP  
602 regime. Using the same approach with the alternative SEVIRI active fire products, we find  
603 that the WFABBA products also show slightly higher errors of omission and commission  
604 than when examined at the fire cluster scale, now being 7% (commission) and 90%  
605 (omission) respectively in comparison to the MODIS product. The error rates for FDeM and  
606 FIR products are, however, very similar when examined on a fire cluster basis to the results

607 on a per fire pixel basis, with a commission rate of 6% for both and an omission rate of 96%  
608 and 95% for FDeM and FIR respectively.

609

## 610 **4. FRP GRIDDED Product Evaluation**

611

### 612 **4.1 Method**

613 Section 2.2 detailed how the LSA SAF SEVIRI FRP-GRID product uses a series of  
614 regionally-specific bias adjustment factors ( $\alpha$ ) to upwardly adjust regional FRP estimates for  
615 e.g. the impact of undetected low FRP fire pixels. The aim is to produce an hourly, regional  
616 FRP estimate that has minimal bias compared to if MODIS had been able to view the same  
617 area at the same time. Full details of the FRP-GRID processing chain are included in Wooster  
618 *et al.* (2015). We evaluated the performance of the applied bias adjustments using a  
619 validation dataset composed of coincident SEVIRI and MODIS observations collected  
620 between May 2008 and May 2009 in each of the four LSA SAF geographic regions.  
621 Boundaries of the relevant MODIS level 2 swath products were used to identify all MODIS  
622 granules that intersected each region during the year-long study period, and fire pixels subset  
623 from the full MODIS ‘MOD14’ and ‘MYD14’ products using six, non-overlapping 5.0° grid  
624 cells arranged in the centre of each MODIS granule (Figure 6). Active fire pixels detected by  
625 MODIS outside of this region of interest were discarded and not used during the analysis.  
626 The sampling design ensured complete coverage of the 5.0° grid cells regardless of the  
627 MODIS ground track, and also mitigated the effects of image distortion at the edge of the  
628 MODIS swath. All MODIS granules collected during the year-long study period were  
629 matched to the most concurrent SEVIRI image, always within  $\pm 6$  minutes of each other. The  
630 same 5.0° grid cells inscribed within the MODIS granule were then used to clip SEVIRI fire  
631 pixels from both (i) the most coincident SEVIRI timeslot, and (ii) the three SEVIRI timeslots  
632 immediately preceding the MODIS overpass. Again, active fire pixels detected by SEVIRI  
633 outside of this region of interest were not included in the analysis. Entire grid cells were also  
634 discarded if three consecutive SEVIRI imaging timeslots could not be retrieved prior to the  
635 SEVIRI timeslot concurrent with the MODIS overpass (i.e., if four imaging timeslots were  
636 not available). This sampling design not only permitted a genuine comparison of coincident  
637 SEVIRI and MODIS observations of FRP, but also mimicked the hourly temporal resolution  
638 of the gridded FRP product.

639

640 After the SEVIRI and MODIS fire pixels were spatially and temporally accumulated, half of  
641 the concurrent and collocated 5.0° grid cells in each region were used to generate the  
642 validation dataset. Relationships between the atmospherically corrected FRP observed by  
643 SEVIRI and MODIS were directly compared among the 5.0° grid cells contained within this  
644 dataset. Rather than using the instantaneous FRP observed by SEVIRI at the timeslot most  
645 concurrent with the MODIS overpass however, the mean FRP generated from the SEVIRI  
646 data available over the preceding hour was used instead to correspond more appropriately  
647 with the hourly resolution of the FRP-GRID product.

648

## 649 **4.2 Results**

650 A complete summary of the FRP-GRID product validation results derived from the  
651 methodology detailed in Section 3.1 is provided in Table 3. Application of the weighted least  
652 squares (WLS) coefficients in northern and southern Africa to the validation dataset yielded  
653 unbiased estimates of the instantaneous FRP that would have been measured by MODIS at  
654 5.0° spatial resolution (e.g., Figure 7a, Table 3). As expected, however, the region-specific  
655 coefficients for South America (Same) and Europe (Euro) geographic regions did not perform  
656 as well. Although the adjustment procedure provides an unbiased estimate of the FRP that  
657 MODIS would have measured in South America, the coefficient of determination ( $r^2$ )  
658 indicates that confidence in the predictive capability of the model is limited at this spatial and  
659 temporal resolution. As a caveat, however, the validation results in South America and  
660 Europe are influenced by observations when SEVIRI did not detect a single active fire pixel  
661 within a 5.0° grid cell during the hour. After removing 5.0° grid cells that only contained an  
662 active fire pixel detected by a single sensor (i.e., thereby forcing a comparison between  
663 observations in which both SEVIRI and MODIS viewed a fire) the  $r^2$  improved to 0.43 in the  
664 South America region. Furthermore, by removing a lone outlier improved the correlation  
665 coefficient slightly further to 0.55. Likewise for Europe, only including observations in which  
666 SEVIRI and MODIS simultaneously detected an active fire pixel yielded an  $r^2$  of 0.31.

667

668 Of course, the linear bias adjustments applied in the FRP-GRID product only capture the  
669 underlying macroscopic features of the sensor-to-sensor relationships, and do not account for  
670 any temporal variability in the SEVIRI-to-MODIS ratios of FRP induced by diurnal or  
671 seasonal fluctuations in fire activity (e.g. as seen in Freeborn *et al.*, 2009). By deriving  
672 different regression coefficients for each of the four LSA SAF regions, however, the FRP-  
673 GRID algorithm does account for broad spatial differences in the sensor-to-sensor

674 relationships that potentially arise from (i) differences in fire regimes, and (ii) differences in  
675 SEVIRI view zenith angles.

676

677 To assess the predictive capability of the bias adjustment factors at broader spatial and  
678 temporal scales than simply the hourly/5° spatio-temporal resolution of the FRP-GRID  
679 product, the SEVIRI and MODIS validation data were accumulated over weekly intervals  
680 and comparisons were performed at scale of the LSA SAF geographic regions. Figure 7b  
681 illustrates that in southern Africa, the bias adjustment factors used to generate the FRP-GRID  
682 product consistently underestimate the weekly sum of FRP measured by MODIS across this  
683 region, and that these results are typical of all four regions (Table 3). Again, this systematic  
684 underestimation is partly attributed to the challenge of performing a bias adjustment when  
685 SEVIRI does not detect a fire pixel (i.e. the linear bias adjustment coefficient is then applied  
686 to an FRP of zero). Nevertheless, the weekly/regional biases shown in Table 3 could in turn  
687 be used to adjust the SEVIRI FRP-GRID product measurements to deliver unbiased estimates  
688 of the FRP that would have been measured by MODIS at the regional/weekly scale.

689

## 690 **5. EXAMPLE APPLICATION OF THE LSA SAF METEOSAT SEVIRI FRP** 691 **PRODUCTS IN THE COPERNICUS ATMOSPHERE MONITORING SERVICE** 692 **(CAMS)**

693

### 694 **5.1 Introduction to FRP-PIXEL Product use in Atmospheric Transport Models**

695 From the FRP-PIXEL product evaluation and inter-comparison conducted in Section 3 it is  
696 apparent that the FRP-PIXEL product detects a larger proportion of the ‘true’ landscape-scale  
697 fire activity than do alternative SEVIRI-derived active fire products, albeit with a higher  
698 commission rate. That evaluation also highlighted the failure of the FRP-PIXEL product to  
699 detect many of the actively burning fires that MODIS would detect, particularly the lower  
700 FRP fires, resulting in an overall omission rate of 77% over the four geographic regions  
701 (Table 1). The degree of difference between geostationary and polar-orbiting active fire  
702 products does, however, vary with factors such as geographic location, season and time of  
703 day (which all influence the type of fire regime and its subcomponents being sampled),  
704 sensor viewing geometry, land cover heterogeneity, fire detection algorithm and the quality  
705 of ancillary data such as cloud masks (Freeborn *et al.*, 2014a; Schroeder *et al.*, 2008; Roberts  
706 and Wooster, 2014; Xu *et al.*, 2010). Indeed, under some conditions, geostationary active fire

707 datasets compare rather favourably against those derived from polar-orbiting sensors.  
708 Georgiev and Stoyanova (2013) analysed a series of short-lived wildfires in south-eastern  
709 Europe with the FRP-PIXEL product, and found the higher temporal resolution of SEVIRI  
710 resulted in a 50% lower active fire omission rate than did the use of MODIS. Wooster *et al.*  
711 (2015) also demonstrate that, taking the Central African Republic as an example, most fires  
712 detected by the MODIS are detected by the SEVIRI FTA algorithm, just not necessarily at  
713 the same time as the fire is detected by MODIS. Indeed, the high temporal frequencies  
714 offered by geostationary observations can enable the diurnal fire cycle and related short-term  
715 changes in fire activity to be far better characterised than with polar-orbiting data, and this  
716 ability is starting to be exploited to parameterise wildfire emissions in atmospheric transport  
717 models.

718  
719 One such example is provided by Baldassarre *et al.* (2015), who used the FRP-PIXEL  
720 products (Wooster *et al.*, 2015) and the WFABBA SEVIRI products (Zhang *et al.*, 2012),  
721 along with MODIS-derived information from the Global Fire Assimilation System (GFAS)  
722 inventory of Kaiser *et al.* (2012), to derived biomass burning emissions inputs for simulations  
723 of emissions from a large fire in Turkey (Antalya, 2008). The FRP-PIXEL product provided  
724 by far the most accurate description of the emissions, both with regard to their spatio-  
725 temporal variation and their absolute magnitude. Unlike the MODIS-derived GFAS  
726 inventory, the SEVIRI FRP-PIXEL product was able to capture the fires complete life cycle,  
727 including the time of peak emissions intensity. And compared to the WFABBA product, the  
728 FRP-PIXEL product produced information more consistent with that from MODIS when  
729 both SEVIRI and MODIS viewed the Antalya region simultaneously. The simulated smoke  
730 plume produced by ingesting the FRP-PIXEL data into the Community Multi-scale Air  
731 Quality (CMAQ) atmospheric chemistry model compared far better with observations of  
732 MODIS-derived aerosol optical depth (AOD), and with carbon monoxide and ammonia  
733 column totals provided by the Infrared Atmospheric Sounding Interferometer (IASI), in  
734 particular in relation to the diurnal variability of the fire emissions and the spatial distribution  
735 and peak concentrations of the smoke. Please refer to Baldassarre *et al.* (2015) in this  
736 Monitoring Atmospheric Composition and Climate (MACC) special issue for further  
737 information on the simulation and inter-comparison. Here we provide a second European  
738 demonstration of the value of geostationary FRP data in the parameterising of wildfire

739 emissions for use in atmospheric transport models, building on a previous more limited study  
740 conducted by Kaiser *et al.* (2009b).

741

## 742 **5.2 Methodology for modelling emissions and transport of smoke from the 2007 Greek** 743 **'mega fire' event**

744

745 We use the FRP-PIXEL product as the basis for calculating smoke emissions to the  
746 atmosphere from a catastrophic 'mega fire' event that occurred around the Mediterranean, in  
747 particular focused on the Greek island of Peloponnese, in August and September 2007. We  
748 use these emissions within components of the CAMS modelling systems to simulate the  
749 transport and fate of the emitted smoke, ultimately estimating the level of human exposure to  
750 high levels of particulate matter (PM<sub>2.5</sub>). The Peloponnese wildfires occurred after a period  
751 of prolonged drought (Gitas *et al.*, 2008), and during a heatwave (Theoharatos *et al.*, 2010).  
752 The MODIS burned area product (Roy *et al.*, 2005) indicates they burned across an area of  
753 around 1847 km<sup>2</sup> (Figure 8), a figure in good agreement with burned area reports provided by  
754 the local Hellenic fire brigade (1899 km<sup>2</sup>). The Peloponnese fires predominantly occurred in  
755 forested land, both coniferous and broadleaved forest, though some areas of shrublands,  
756 grasslands and olive groves were also affected (Veraverbeke *et al.*, 2010; Koutsias *et al.*,  
757 2012). Such was their severity that 0.32 Tg (40 %) of the estimated mean annual carbon  
758 monoxide (CO) emissions for Greece overall were estimated to have been released by these  
759 fires alone (Turquety *et al.*, 2009). The fires contributed greatly to reductions in local air  
760 quality, with PM<sub>10</sub> values in Athens reaching almost 100 µg m<sup>-3</sup>, double that of the European  
761 Union Ambient Air Quality Standard for daily PM<sub>10</sub> (50 µg m<sup>-3</sup>). Outside Athens at a  
762 background non-urban site, on 24-25<sup>th</sup> August the PM<sub>10</sub> concentration rose to 49 µg m<sup>-3</sup>,  
763 significantly up from the 19 µg m<sup>-3</sup> measured the day before (Liu *et al.*, 2009). Marlier *et al.*  
764 (2014) and Reid *et al.* (2009) have already highlighted the potential improvements that high  
765 temporal resolution source information can have on the modelling of biomass burning  
766 emissions transport, and the exceptional and strongly varying intensity of the Peloponnese  
767 fires provides an excellent opportunity to demonstrate this further using SEVIRI-derived FRP  
768 observations.

769

### 770 **5.2.1 Derivation of smoke emissions fields from FRP-PIXEL data**

771

772 FRP-PIXEL data of the European LSA SAF geographic region collected between the 1<sup>st</sup>  
773 August and 13<sup>th</sup> September 2007 was examined for signals of the fires that occurred around  
774 the Mediterranean during July - Aug 2007. Clear FRP signals were apparent from these fires,  
775 particularly those on Peloponnese, but it was also evident that the adjusted version of Cloud  
776 Mask (CMa) of Derrien and Le Gleau (2005) delivered by the Nowcasting and Very Short  
777 Range Forecasting SAF (NWC SAF; [www.nwcsaf.org](http://www.nwcsaf.org)) and used within the FRP-PIXEL  
778 product processing chain (Wooster *et al.*, 2015) was identifying some of the extremely thick  
779 smoke emitted by these fires as cloud. This is appropriate for studies requiring clear sky  
780 observations, but the sensitivity of the algorithm for detecting cloud or smoke contaminated  
781 pixels can occasionally result in the omission of fire activity. Since cloud masking is one of  
782 the first things conducted within the FRP-PIXEL product processing chain (Wooster *et al.*,  
783 2015), misidentification of very thick smoke as cloud prevents fires being identified in these  
784 pixels using the FTA algorithm, even though we know that active fires can be quite reliably  
785 detected through even quite thick smoke (Petitcolin and Vermote, 2002). This is because  
786 smoke particles have a diameter typically much smaller than the wavelength of the MWIR  
787 band and so do not act as strong scatterers of the fire-emitted radiation, unlike meteorological  
788 cloud (Kaufman and Remer, 1994). Analysis of the raw SEVIRI level 1.5 data, along with the  
789 EUMETSAT Meteorological Product Extraction Facility (MPEF) cloud mask (Tjemkes and  
790 Schmetz, 1997), confirmed the identification of some areas of thick smoke as cloud by the  
791 CMa cloud mask, and also confirmed that the true median percentage cloud cover over  
792 Peloponnese was low over the period of the mega fire event (13%). To prevent the masking  
793 out of smoke covered fires, which also then impacts surrounding pixels due to the single pixel  
794 wide mask that is applied around cloud and water pixels (Wooster *et al.*, this issue), for this  
795 particular application we decided to turn off the use of the adjusted CMA cloud mask, and  
796 simply relied on the basic cloud masking tests used within the FTA algorithm itself (Wooster  
797 *et al.*, 2015). Currently investigations are ongoing to make the cloud masking within the  
798 FRP-PIXEL product less sensitive to thin cloud and other atmospheric phenomena through  
799 which fires can still be identified, including very thick smoke (Wooster *et al.*, 2015).

800

801 We then gridded the FRP data from within the FRP-PIXEL product to 0.1° grid cells and  
802 calculated the mean FRP for each cell at an hourly temporal resolution. As with the  
803 operational version of the Global Fire Assimilation System (GFAS; Kaiser *et al.*, 2012), the

804 FRP density ( $\tilde{q}_j$ ,  $\text{Wm}^{-2}$ ) for each cell was then calculated by normalising the measured FRP  
 805 by the grid cell area ( $a_j$ ,  $\text{m}^2$ ):

806

$$\tilde{q}_j(d, h) = \frac{1}{a_j} \frac{1}{4} \sum_{k=0,15,30,45} \sum_{i_k \in j} F_{ik}(d, h) \quad (1)$$

807

808 where  $d, h$  and  $k$  are the date, hour and minute of the SEVIRI observations respectively,  $\sum F_{ik}$   
 809 is the summation of all FRP measurements within grid cell  $j$ .

810

811 The rate of dry matter (DM) fuel consumption ( $\varphi$  [ $\text{kg s}^{-1} \text{m}^{-2}$ ]) was derived from the FRP  
 812 density measures of each grid cell ( $\tilde{q}$ ,  $\text{Wm}^{-2}$ ) following the method described in Wooster *et al.*  
 813 *al.* (2005):

814

$$\varphi(d, h) = c \times \tilde{q}(d, h) \quad (2)$$

815

816 where  $d$  is the day,  $h$  is the hour and  $c$  is the conversion factor that relates fuel consumption  
 817 to FRP and which is  $0.368 \pm 0.015$  ( $\text{kg MJ}^{-1}$ ; Wooster *et al.*, 2005). The approach was further  
 818 developed with land cover dependent adjustments by Kaiser *et al.* (2012). However, we  
 819 maintain the original fuel consumption estimation and adjust the emission fluxes at the level  
 820 of the emission factors, see section 5.2.2.

821

### 822 **5.2.2 FRP-derived aerosol emissions and atmospheric modelling**

823

824 Ichoku and Kaufmann (2005) first developed an approach to estimate aerosol emissions using  
 825 FRP and aerosol optical depth (AOD) measurements using ‘*coefficients of emission*’ that  
 826 related FRP to total particulate matter (TPM) as a function of land cover type. The approach  
 827 implemented herein calculates emissions using the DM fuel consumption rate  $\varphi$  ( $\text{kg s}^{-1} \text{m}^{-2}$ ):

828

$$\Phi_s(d, h) = \eta_s \times \varphi(d, h) \quad (3)$$

829

830 where  $\Phi_s$  is the emission flux density ( $\text{kg s}^{-1} \text{m}^{-2}$ ) of species  $s$ ,  $d$  is the day,  $h$  is the hour and  
 831  $\eta$  is the emissions factor ( $\text{kg kg}^{-1}$ ) given by :

832

$$\eta_s = \alpha(s) \times \kappa_l(s) \quad (4)$$

833

834 where  $\kappa_l$  is the land cover ( $l$ ) specific emissions factor for species  $s$  and  $\alpha$  is a constant which  
835 is used to adjust bottom-up aerosol emissions estimates to those observed in top-down  
836 inventories. A regionally varying bias occurs between bottom-up derived aerosol emissions  
837 and MODIS AOD measurements, requiring the former to be adjusted when being used in air  
838 quality or climate model simulations (Peterenko *et al.*, 2012). Yang *et al.* (2011) also found  
839 smoke emissions ( $PM_{2.5}$ ) derived using the bottom-up approach was underestimated by a  
840 factor of three when compared to MODIS AOD retrievals. Kaiser *et al.* (2012) recommend a  
841 global aerosol enhancement by a factor of 3.4 as first-order correction. These values are also  
842 broadly consistent with differences of up to a factor of three found by Ichoku and Kaufmann  
843 (2005) using satellite observations of FRP and AOD compared to measurements of  $c \times \kappa_l(s)$   
844 derived from laboratory measurements. Here, we estimate emissions of organic matter and  
845 black carbon in exact agreement with Ichoku and Kaufmann (2005) by enhancing their  
846 emission factors for Andreae and Merlet (2001) with a factor of 3.1. According to the  
847 GFEDv3 land cover dataset, also used for our calculations in GFAS (Kaiser *et al.*, 2012), the  
848 fire affected region of Greece is classed as extratropical forest and the emitted species and  
849 relevant emissions factors are given in Table 4.

850

851 The atmospheric aerosol model (Morcrette *et al.*, 2008) used within the ECMWF Integrated  
852 Forecasting System (IFS) represents smoke aerosols as black carbon (BC) and organic matter  
853 (OM), of both hydrophilic and hydrophobic types. Emissions of the latter are approximated  
854 by scaling organic carbon (OC) emissions estimates by a factor of 1.5. Other aerosols  
855 included in the modelling are sea salt, dust and sulphate aerosols, and advection, convection,  
856 diffusion, dry and wet deposition and chemical conversion of these aerosols are simulated,  
857 with meteorology nudged to the operational ECMWF analysis every 12 hours. The aerosol  
858 abundance however, is based solely on source and sink processes and the atmospheric  
859 transport. In this study the IFS model was run with a horizontal resolution of 25 km (T799)  
860 and with 91 vertical levels up to 0.01 hPa.

861

862 Smoke emissions from the Peloponnese fires were calculated using Equations 3 and 4, along  
863 with the emissions factors given in Table 4. The smoke emissions must be injected into the  
864 atmosphere at a particular height, or distribution of heights, and such injection height

865 assumptions can have implications for the resulting spatio-temporal distribution of the  
866 emitted species. Leung *et al.* (2007) and Guan *et al.* (2008) demonstrated that use of more  
867 detailed plume injection height assumptions resulted in a reduction in near surface CO  
868 concentrations, since more plumes were assumed to be lofted above the boundary layer.  
869 Paugam *et al.* (2015a) provided a recent review of approaches to estimate smoke plume  
870 injection height, including the methods of Sofiev *et al.* (2012) and Paugam *et al.* (2015b) that  
871 use FRP measurements to characterise wildfire thermal properties related to plume rise. This  
872 research remains at a relatively early stage, but it appears that FRP measures may indeed  
873 have a role to play in characterising smoke plume injection height as well as the rate of  
874 emission of chemical and aerosol species. Here we retained the commonly used assumption  
875 that the calculated smoke emissions are injected into the lowest atmospheric level, since this  
876 is generally what has been assumed in the series of MACC projects thus far (Kaiser *et al.*,  
877 2012). The CAMS is anticipated to use injections heights from Paugam *et al.* (2015b) in the  
878 future.

879

## 880 **5.3 Results**

881

### 882 **5.3.1 Fuel consumption during the Peloponnese Wildfires**

883

884 Figure 9a illustrates the temporal dynamics of total fire FRP (MW) and the equivalent rate of  
885 fuel consumption ( $\text{tonnes s}^{-1}$ ), calculated from the MODIS and SEVIRI FRP measurements at  
886 their native temporal resolutions. The period of greatest fire activity occurs between the 23<sup>rd</sup>  
887 and 27<sup>th</sup> August, where the initial active fire detections made by SEVIRI and MODIS occur  
888 at 07:57 and 09:00 (UTC) respectively (23<sup>rd</sup> August). At their most intense, the Peloponnese  
889 fires consumed over 15  $\text{tonnes s}^{-1}$  of biomass, and such was their intensity that large  
890 quantities of fuel ( $> 3 \text{ tonnes s}^{-1}$ ) were consumed even during the night, a period when more  
891 landscape typically fires die down quite considerably due to less fire-conducive ambient  
892 conditions (Roberts and Wooster, 2007; Roberts *et al.*, 2009). The temporally intermittent  
893 MODIS Terra and Aqua FRP measurements broadly capture the pattern seen in the much  
894 more frequent SEVIRI data, and are typically much higher in magnitude. On the 25<sup>th</sup> August,  
895 MODIS Aqua (12:05 UTC) detects a total FRP exceeding 180 GW, with the SEVIRI FRP  
896 (12:12 UTC) very much lower (38 GW). The large difference mainly derives from the fact  
897 that whilst 10% (31) of the MODIS active fire pixels have an FRP  $> 1600$  MW and 5%  $> 3000$   
898 MW, 23% of the 100 active fire pixels detected by the FRP-PIXEL product are in fact

899 saturated in the SEVIRI MWIR channel. Between the 24<sup>th</sup> and 26<sup>th</sup> August, when the  
900 wildfires were most intense, MODIS made 13 overpasses and the unadjusted SEVIRI  
901 observations measured 39% of the total FRP measured by MODIS. This demonstrates the  
902 massive scale and intensity of these fires, particularly given that SEVIRI's pixel area at this  
903 location is around 14 km<sup>2</sup>.

904

905 Temporal integration of the SEVIRI FRP measurements between the 23<sup>rd</sup> August and 3<sup>rd</sup>  
906 September indicates an energy release of 4.73 PJ which, following Equation 2, equates to  
907 1.74 Tg of combusted fuel, predominantly consumed on 23 - 27 August (Figure 9b). Various  
908 burned area estimates exist for the Peloponnese fires, including 1773 km<sup>2</sup> (Gitas *et al.*, 2008),  
909 1628 km<sup>2</sup> (European Forest Fires Information System, EFFIS; European Commission, 2010)  
910 and 1847 km<sup>2</sup> (Roy *et al.*, 2005; Figure 8). Dividing the SEVIRI-FRP derived fuel  
911 consumption with these burned areas provides mean dry matter (DM) fuel consumptions of  
912 0.98 kg m<sup>-2</sup>, 1.07 kg m<sup>-2</sup> and 0.94 kg m<sup>-2</sup> respectively. Aleppo pine forests occupy around  
913 370,000 ha in Greece and are abundant on Peloponnese (Verroios and Georgiadis, 2011).  
914 Mitsopoulos and Dimitrakopoulos (2013) assessed 40 stands in this fuel type and found  
915 canopy fuel loads to range between 0.63 and 1.82 kg m<sup>-2</sup>, estimating a mean of 1.08 kg m<sup>-2</sup>.  
916 Using the maximum fuel load (1.82 kg m<sup>-2</sup>), the three burned area estimates (1773 km<sup>2</sup>,  
917 1628km<sup>2</sup> and 1847km<sup>2</sup>), and assuming a combustion completeness value for forest of 0.6  
918 (van der Werf *et al.*, 2006) we calculated a fuel consumption for these fires of 1.94 Tg, 1.77  
919 Tg and 2.01 Tg respectively using the standard burned area based approach (Seiler and  
920 Crutzen, 1980), which is similar to our SEVIRI-derived estimate of 1.74 Tg. Turquety *et al.*  
921 (2009) estimates that 0.32 Tg of CO was emitted during the Peloponnese fires, which using  
922 the emissions factors given in Table 4 results in a larger top-down derived fuel consumption  
923 3.0 Tg (with a stated uncertainty of ~30%). Due to the aforementioned SEVIRI MWIR  
924 channel saturation, the SEVIRI FRP-derived fuel consumption estimate is considered a  
925 minimum estimate.

926

### 927 **5.3.2 Smoke Plume Evolution**

928

929 The Peloponnese wildfires produced huge volumes of smoke that affected regional air quality  
930 in the Eastern Mediterranean (Poupkou *et al.* 2014). Figure 10a shows a true colour  
931 composite image derived from MODIS Terra imagery acquired on the 26<sup>th</sup> August 2007  
932 (09:35 UTC). The mirrored 'S' shaped plume present over the Mediterranean extends across

933 to Tunisia at this time. Figure 10b shows a snapshot of the modelled smoke emissions derived  
934 from our use of the FRP-PIXEL product dataset to derive the wildfire emissions, and the use  
935 of these within the IFS model (Section 5.2). The modelled smoke emission transport captures  
936 the spatial structure of the advected smoke plumes very well, consisting of a series of ‘pulses’  
937 of increased AOD that result from the particularly intense emissions during the peak of each  
938 diurnal fire cycle. The large region of particularly high AOD on the coast of Libya (L on  
939 Figure 10b, and shown in Figure 11a and 11b) results from the intense fire emissions on the  
940 25<sup>th</sup> August, where more than 18 tonnes s<sup>-1</sup> of biomass were apparently being consumed at the  
941 peak intensity. To the west of the main smoke plume, a thinner plume with a lower AOD is  
942 evident emanating from fires in Albania. To the east, a smaller plume resulting from wildfires  
943 in Turkey is also captured.

944

945 It is evident from Figure 10 that the modelled smoke plumes are offset slightly compared to  
946 the actual plumes observed by MODIS, and this is most evident over the Libyan coast. The  
947 difference is believed to result from injecting the smoke plume into the lowest atmospheric  
948 level, which is an oversimplification as stated earlier since MISR-derived smoke plume  
949 heights acquired on 26<sup>th</sup> August indicated that the plume closest to the wildfires had a height  
950 of 2.5 km (Lui *et al.*, 2009) and CALIPSO lidar observations have detected the plumes at  
951 altitudes of 2-3 km on 25<sup>th</sup> and 26<sup>th</sup> August (Turquety *et al.* 2009). In contrast, the simulated  
952 plumes are located predominantly below 1 km (not shown). Global analysis of MISR data  
953 indicates that a large proportion wildfire smoke plume heights remain beneath the boundary  
954 layer, although particularly intense fires can inject smoke into the free troposphere (Val  
955 Martin *et al.*, 2010; Dirksen *et al.*, 2009; Fromm *et al.*, 2000). Our modelled plume is  
956 typically also broader than that observed by MODIS, and covers a larger spatial extent. This  
957 may result from the relatively coarse spatial resolution used in the model, and comparisons  
958 between our simulation and MODIS AOD estimates made on the 26<sup>th</sup> August (DOY 238,  
959 Figure 11a and b) indicate that whilst the broad magnitude of the modelled smoke emission  
960 ‘pulses’ are in good agreement with observations, the simulated plumes AOD appears  
961 overestimated compared to MODIS. This suggests some inaccuracies remain in the aerosol  
962 source modelling, and for example Garcia-Menendez *et al.* (2014) found modelled PM<sub>2.5</sub>  
963 concentrations are more sensitive to the injection height parameterisation rather than to the  
964 emissions vertical distribution, due to the diurnal evolution of the planetary boundary layer  
965 and local meteorological conditions.

966

#### 967 **5.4. Impact of Emissions Fields Temporal Resolution**

968

969 A number of studies (e.g. Chen *et al.*, 2009; Marlier *et al.*, 2014; Reid *et al.*, 2009; Garcia-  
970 Menendez *et al.*, 2014) have found that resolving the diurnal variability of fire emissions has  
971 important implications when modelling the emissions atmospheric transport. We used our  
972 study of the Peloponnese fires to address this issue by reducing the temporal resolution of the  
973 SEVIRI FRP-derived emissions density fields, from the original 1-hour to 1-day and then 1-  
974 week, the latter two being more representative of the global emissions inventories developed  
975 using only observations from polar orbiting instruments (van der Werf *et al.*, 2010; Kaiser *et*  
976 *al.*, 2012; Sofiev *et al.*, 2009). The resulting sensitivity to temporal resolution is illustrated in  
977 Figure 12a and b, which show modelled AOD (at 550nm) on the 26<sup>th</sup> August (09:35 UTC)  
978 using the emissions prescribed at a daily and weekly temporal resolution. In both cases, the  
979 shape of the modelled Peloponnese smoke plume remains broadly consistent with the hourly  
980 simulation of Figure 10a, although smoke emissions from neighbouring countries are much  
981 less pronounced. The Albanian plume is progressively shorter in Figure 12a and 12b, whilst  
982 some plumes (e.g. those from Turkey to Crete) are missing altogether. Source emissions at  
983 weekly temporal resolution (Figure 12b) remove the daily variability, resulting in lower  
984 aerosol amounts at both the source region and over the entire plume. It is also evident that  
985 emissions are being generated at incorrect times when using these reduced temporal  
986 resolution source data. For example, the daily and weekly simulations have plumes  
987 emanating from southern Italy too early, since fires are in fact in reality just developing in the  
988 source region (Figure 12b). Baldassarre *et al.* (2015) provide further evidence of the  
989 importance of the high temporal resolution provided by the SEVIRI FRP-PIXEL dataset  
990 when modelling smoke transport from individual large fire events.

991

#### 992 **5.5 Comparison of *in-situ* and modelled aerosol optical depth**

993

994 Section 5.4 has indicated that model simulations using hourly smoke emissions fields  
995 improve the representation of both the spatial and temporal evolution of the smoke plumes  
996 from the main Mediterranean mega-fires of August 2007. However, qualitative comparison  
997 to MODIS AOD estimates (Figure 11 a,b) indicated that the plumes modelled AOD was  
998 somewhat higher than satellite derived AOD estimates. Over the same time period as the  
999 Peloponnese fires, a series of fires occurred on the Algerian coast (Figure 13a) whose plumes  
1000 were detected by the AERONET (Holben *et al.*, 2001) site at Lecce (Italy; 40.35°N,

1001 18.16°E). Figure 13b and c show the modelled smoke and dust AOD respectively on the 31<sup>st</sup>  
1002 August (00:00 UTC) where the former illustrates the smoke plume extension over the  
1003 AERONET site (yellow star symbol). Figure 13d is a temporal profile of AOD recorded (at  
1004 500 nm) over Lecce from AERONET observations of total (red circles) and fine mode  
1005 (orange circles) AOD, daily averaged MODIS AOD (550 nm) observations (black triangles)  
1006 and model simulations of total AOD (blue line). Modelled AOD contributions of smoke  
1007 (purple line) and dust (green line) to the total AOD are also shown. The MODIS AOD  
1008 estimates are derived through averaging all observations within the model grid cell. The  
1009 smoke AOD displays greater short term variability than does the dust AOD, since the  
1010 wildfires represent significantly more localised sources than do the regions of dust uplift. The  
1011 smoke AOD displays an increase in magnitude from 0.6 to 1.3 between the 31<sup>st</sup> August and  
1012 1<sup>st</sup> September, which occurs 23 hours prior to the peak FRP (63 GW) of the Algerian fires.  
1013 However, between the 27<sup>th</sup> and 31<sup>st</sup> August, MODIS detected 330 active fires in southern  
1014 Italy (Figure 14) which were greatest in number on the 27<sup>th</sup> (114) and 31<sup>st</sup> (110) August and  
1015 which are likely to have contributed to the Algerian smoke plume but which may not all be  
1016 included in our modelling since the majority (63%) had an FRP <30 MW and so may not be  
1017 detected by SEVIRI.

1018  
1019 Compared to the daily averaged MODIS AOD, our modelled total AOD is typically  
1020 overestimated by ~20% during the overpass of the smoke plume (31<sup>st</sup> August), but the model  
1021 does capture the temporal trend of the observed AOD rather well. The AERONET AOD data  
1022 provides a more complete temporal profile than do MODIS' AOD observations, and our  
1023 modelled total AOD typically captures these dynamics. However, the onset of increased  
1024 AOD due to the Algerian fires (30<sup>th</sup> August) is captured 8 hours earlier by AERONET than  
1025 by our modelled AOD, whilst the descending limb is temporally coincident between datasets.  
1026 The former may result from assumptions made regarding the smoke plume injection heights,  
1027 or to shortcomings in the simulations due to increased cloud cover over Algeria on the 29<sup>th</sup>  
1028 August. It is also possible that, given the rapid rise in AOD in a three hour period, this is a  
1029 localised effect due small, undetected fires in the vicinity of the AERONET station and  
1030 which are not represented in our simulation. Between the 28<sup>th</sup> and 29<sup>th</sup> August, MODIS  
1031 detected 96 active fires (Figure13, red symbols) to the south-west of Lecce and in close  
1032 proximity to the smoke plume emitted by the Algerian fires, and these most likely to  
1033 contribute to the elevated AOD at this time (Figure 11a and b). In general, the AOD resulting  
1034 from the use of the SEVIRI FRP-PIXEL product data and the IFS model is overestimated

1035 compared to AERONET observations by 10 - 40% during the biomass burning plume  
1036 overpass, and with a discrepancy of 8 hours at the onset of the plume overpass. Clearly we  
1037 will in future aim to further refine the fire emissions parameterisation, which appears  
1038 currently to be positively biased relative to the observations. Nevertheless, this case study has  
1039 demonstrated the clear value of the high temporal frequency SEVIRI-derived FRP  
1040 observations for large, rapidly varying wildfires such as this.

1041

## 1042 **5.6 Air quality assessment**

1043

1044 The 2007 Mediterranean 'mega fire' event significantly impacted regional air quality, and  
1045 fires worldwide are known to have severe health implications for those badly affected by  
1046 their emissions. Jacobson (2014) estimated that average annual premature mortalities due to  
1047 biomass burning emissions of PM<sub>2.5</sub> and ozone are of the order of 20,000 (10,000-30,000) and  
1048 230,000 (63,000-405,000) respectively, equating to between 5 and 10% of global mortality  
1049 due to indoor and outdoor air pollution. One of the primary uses of the CAMS is to forecast  
1050 regional air quality across Europe, providing rapid and reliable information directly relevant  
1051 to human health issues, and this includes the consequences of wildfire emissions  
1052 (Hollingsworth *et al.*, 2008). It is therefore pertinent to assess the significance of our  
1053 Peloponnese smoke emissions transport simulations in relation to air quality and human  
1054 health, potentially since Mitsakis *et al.* (2014) already estimated that over 2000 people were  
1055 admitted to hospitals and medical centres as a direct result of the Peloponnese fire event, and  
1056 of these 1100 were due to cardio-vascular and respiratory problems. The World Health  
1057 Organisation (WHO) air quality guidelines (WHO, 2006) in particular set a limit of 25 µg m<sup>-3</sup>  
1058 for the concentration of fine mode particulate matter (PM<sub>2.5</sub>) averaged over a 24 hour period.  
1059 We estimated concentrations of PM<sub>2.5</sub> using our simulated OM and BC concentrations in the  
1060 lowest modelled atmospheric layer, and calculated the 24-hour running average for  
1061 comparison to this WHO threshold.

1062

1063 Figure 15 shows the distribution of 24-hour mean PM<sub>2.5</sub> concentrations modelled between  
1064 23<sup>rd</sup> August and 3<sup>rd</sup> September (when the Peloponnese wildfires were at their most intense;  
1065 Figure 9a). It is clear that the impacts of the Peloponnese wildfires extend well beyond  
1066 Greece's national borders, and indeed resulted in large parts of the Mediterranean region  
1067 exceeding the WHO 25 µg m<sup>-3</sup> PM<sub>2.5</sub> concentration threshold by significant margins. In fact,  
1068 analysis of the spatial distribution of these data with respect to population density (CIESIN

1069 and CIAT, 2005) indicated that, for the region shown in Figure 15, up to 40 million people  
1070 might have been subject to PM<sub>2.5</sub> concentrations exceeding the WHO guidelines. However, it  
1071 should be stressed that this is an upper limit for the exposure, because our study significantly  
1072 over-estimates near-surface smoke concentration due to the assumed boundary-layer injection  
1073 of the emissions. In particular, surface PM<sub>2.5</sub> concentrations in regions reasonably close to the  
1074 source that are well above 100 µg m<sup>-3</sup> are very likely to be spurious, and Liu *et al.* (2009)  
1075 report elevated non-urban values closer to 49 µg m<sup>-3</sup>, albeit still at some distance from source.  
1076 Nonetheless, the spatial range of the affected area, and the considerable human health  
1077 impacts that these type of large wildfire events can have, highlights the necessity of  
1078 modelling their smoke emissions and forecasting their atmospheric transport in the manner  
1079 demonstrated here. Through such work, the CAMS and its downstream services aim at  
1080 improving emergency preparedness through air quality forecasts. Geostationary FRP data are  
1081 likely to be an important component of this system, particularly so as their high temporal  
1082 resolution FRP data provides a unique view of the type of individual large "mega fire" event  
1083 studied here, that can impact regional air quality so dramatically over short timescales.

1084

## 1085 **6.0 SUMMARY AND CONCLUSIONS**

1086

1087 This work has provided a detailed performance evaluation of the Meteosat SEVIRI FRP  
1088 products available from the LSA SAF, both the full resolution FRP-PIXEL product and the  
1089 reduced resolution FRP-GRID product, both available in near real time and in archived form  
1090 (<http://landsaf.meteo.pt/>). It has also provided a detailed example of use of the former product  
1091 in characterising the smoke emissions from a large European wildfire event whose smoke  
1092 significantly affected the Mediterranean region as a whole, and for which we have  
1093 demonstrated an ability to simulate the atmospheric transport and human health impacts at  
1094 high temporal resolution.

1095

1096 When evaluated against the MODIS MOD14 and MYD14 active fire products, the active fire  
1097 pixel detection error of commission of the FRP-PIXEL product is found to be 9% in the  
1098 North African LSA SAF geographic region, and increases to higher values particularly in  
1099 Europe and South America. The basis of this variation is the combination of SEVIRI's  
1100 increasing pixel area with view zenith angle away from the sub-satellite point, and the  
1101 relative proportion of lower intensity and/or smaller fires in the various LSA SAF geographic  
1102 regions (i.e. their fire regimes). Area-based comparisons indicate that the FRP-PIXEL

1103 product underestimates compared to simultaneously collected MODIS FRP of a region by  
1104 between 35 and 89%, with the variation being again dependent upon the above factors.  
1105 Underestimation is typically maximised at regions extending towards the edge of the viewing  
1106 disk, furthest away from the SEVIRI sub-satellite point. However, comparison of the FRP of  
1107 individual fires successfully detected almost simultaneously by both SEVIRI and MODIS  
1108 indicates a strong agreement between the two FRP measurements, with the FRP-PIXEL  
1109 product meeting its Target Accuracy requirements. We find that 76% of the examined  
1110 simultaneously detected fire clusters had an FRP from SEVIRI within 30% of that measured  
1111 by MODIS, which given the recent quantification of MODIS' FRP uncertainty (Freeborn *et*  
1112 *al.*, 2014c) indicates good performance from the FRP-PIXEL product. Overall, minimal bias  
1113 is seen between the per-fire FRP observations made by the two sensors.

1114  
1115 When compared against that of other active fire products derived from the same Meteosat  
1116 SEVIRI observations, the performance of the operational geostationary fire thermal anomaly  
1117 (FTA) algorithm used within the FRP-PIXEL product (Wooster *et al.*, 2015) compares  
1118 favourably. During our comparison to MODIS, the SEVIRI WFABBA, FDeM and FIR  
1119 products from Prins *et al.* (1998), Amraoui *et al.* (2010) and Joro *et al.* (2008) respectively  
1120 have higher active fire errors of omission, varying between 84 and 95%, as compared to the  
1121 77% of the FRP-PIXEL product. However, these alternative SEVIRI-derived active fire  
1122 products do have lower errors of commission than the FRP-PIXEL product when compared  
1123 to MODIS, ranging between 5 and 6% (the FRP-PIXEL product has a 13% commission  
1124 error). The FTA errors of commission are currently being reduced by re-inclusion of the  
1125 dynamic spatial thresholding parameters described in Section 3.2.2 that were removed from  
1126 the operational FTA algorithm for computational speed, but included in the original Roberts  
1127 and Wooster (2008) prototype.

1128  
1129 The Level-3 FRP-GRID product accumulates a series of FRP-PIXEL products and provides  
1130 regional estimates of mean FRP at an hourly temporal resolution and a 5.0° spatial resolution.  
1131 These estimates come already adjusted for cloud cover, and for the impact of the low spatial  
1132 resolution detection bias that results in SEVIRI failing to detect the lower FRP active fire  
1133 pixels. Our evaluation indicates good performance of these bias corrections at the hourly,  
1134 5.0° product resolution, but evaluation of accumulated data against summed weekly MODIS  
1135 FRP over the four LSA SAF geographic regions indicates that the FRP-GRID product  
1136 underestimates total FRP at this scale. This largely results from the difficulty in accounting

1137 for situations where MODIS detects fire activity in a grid cell whilst SEVIRI does not, and so  
1138 the bias corrections remain inactive. We provide herein some additional adjustment factors  
1139 for those wishing to use the SEVIRI FRP-GRID datasets at this type of scale.

1140

1141 Despite their coarse spatial resolution limitations, the FRP products available from  
1142 geostationary satellites offer an unprecedented high temporal resolution for studying wildfire  
1143 emissions. This is a key advantage when using such data to parameterise wildfire smoke  
1144 emissions within atmospheric transport models (Reid *et al.*, 2009). Here we use a version of  
1145 the FRP-PIXEL product to characterise the smoke emissions from the August 2007  
1146 Peloponnese wildfires. The resulting emissions fields are used within ECMWF's Integrated  
1147 Forecast System (IFS) to model the smoke emissions transport, and in particular the black  
1148 carbon and organic carbon aerosols and the resulting aerosol optical depth and PM<sub>2.5</sub> surface  
1149 concentrations. Our results support the findings of other recent studies (e.g. Garcia-Menendez  
1150 *et al.*, 2014; Marlier *et al.*, 2014) in that higher temporal resolution smoke emissions  
1151 estimates provide increased fidelity in the resulting smoke plume aerial distribution and  
1152 optical thickness metrics than do simulations conducted using daily or weekly temporal  
1153 resolution data. Visual assessment of the modelled plumes spatial distribution against  
1154 simultaneous MODIS optical imagery shows good agreement, but the modelled plume is  
1155 slightly offset from the observations which is believed to result from injecting the plume into  
1156 the lowest atmospheric layer (whereas in reality it would have been lofted to higher  
1157 altitudes). Quantitative comparisons between our modelled AOD and the coincident MODIS-  
1158 and AERONET-derived AOD values indicate that modelled AODs are overestimated by ~ 20  
1159 - 30%. Further research into model parameterisation (e.g. injection height) and the aerosol  
1160 emission factors used is required to investigate this bias, particularly so as it is likely that we  
1161 underestimate fuel consumption due to SEVIRI MWIR channel saturation during this  
1162 extreme wildfire event. The European Union (EU) has recently signed a delegation  
1163 agreement with ECMWF to provide the services implemented in MACC, including the FRP-  
1164 based Global Fire Assimilation System (GFAS; Kaiser *et al.*, 2012), in an operational manner  
1165 until at least 2020. This includes on-going developments of GFAS which aim at providing  
1166 emission estimates with an hourly temporal resolution by combining FRP observations from  
1167 both polar orbiting and geostationary satellites. Key pre-requisites are the implementation of  
1168 a model for the diurnal cycle of FRP (Andela *et al.* 2015) and a suitable bias correction for  
1169 geostationary FRP products to account for the omission of low intensity fires, building on the  
1170 simple linear bias corrections applied currently in the FRP-GRID products.

1171  
1172  
1173  
1174  
1175  
1176  
1177  
1178  
1179  
1180  
1181  
1182  
1183  
1184  
1185  
1186  
1187  
1188  
1189  
1190  
1191  
1192  
1193  
1194  
1195  
1196  
1197  
1198  
1199  
1200  
1201  
1202  
1203  
1204

## 7.0 Acknowledgements

Funding for this work came from the UK NERC National Centre for Earth Observation (NCEO), from the LSA SAF project, from EUMETSAT and the EU H2020 project MACC-III (contract no. 633080). SEVIRI data were kindly provided under an ESA/EUMETSAT AO, the MODIS data were provided by the NASA EDC DAACS and the European Forest Fire Information System (EFFIS; <http://effis.jrc.ec.europa.eu>) of the European Commission Joint Research Centre provided burned area data. The GOES\SEVIRI WFABBA data were kindly provided by the Cooperative Institute for Meteorological Satellite Studies (CIMSS) within the Space Science and Engineering Center (SSEC) at University of Wisconsin (UW-Madison) as a collaborative effort between NOAA / NESDIS / STAR and UW-CIMSS personnel. The SEVIRI FRP product were provided by the LSA SAF (<http://landsaf.meteo.pt/>), the FDeM product was provided by Carlos C. DaCamara and Sofia Ermida at Universidade de Lisboa (<http://www.fc.ul.pt/>). The FIR fire products were obtained from EUMETSAT EO portal (<https://eoportal.eumetsat.int/>). The authors would also like to thank Alessio Lattanzio (EUMETSAT), Isabel Trigo (LSASAF) and Yves Govaerts (Rayference) for the assistance and advice provided during this study.

1205 **8.0 References**

1206

1207

1208 Aminou, D. M. A., Jacquet, B. and Pasternak, F. (1997) Characteristics of the Meteosat  
1209 Second Generation Radiometer/Imager: SEVIRI, *Proceedings of SPIE, Europto series*, Vol.  
1210 3221 pages 19-31.

1211

1212 Amraoui, M., DaCamara, C. C. and Pereira, J. M. C. (2010) Detection and monitoring of  
1213 African vegetation fires using MSG-SEVIRI imagery. *Remote Sensing of Environment*. 114.  
1214 1038-1052.

1215

1216 Andela, N., Kaiser, J.K, van der Werf, G., Wooster, M.J. (submitted) New fire diurnal cycle  
1217 characterizations to improve Fire Radiative Energy assessments made from low-Earth orbit  
1218 satellites sampling, *Atmos. Chem. Phys.*, 15(15):8831–8846.

1219

1220 Baldassarre, G., Pozzoli, L., Schmidt, C. C., Unal, A., Kindap, T., Menzel, W. P., Whitburn,  
1221 S., Coheur, P.-F., Kavgaci, A., and Kaiser, J. W. (2015). Using SEVIRI fire observations to  
1222 drive smoke plumes in the CMAQ air quality model: a case study over Antalya in 2008.  
1223 *Atmospheric Chemistry and Physics*, 15(14):8539–8558.

1224

1225 Andreae, M. O., and P. Merlet (2001) Emission of trace gases and aerosols from biomass  
1226 burning. *Global Biogeochemical Cycles*, 15. 4. 995-966.

1227

1228 Berk, A., Anderson, G.P., Acharya, P.K., Bernstein, L.S., Muratov, L., Lee, J., Fox, M.,  
1229 Adler-Golden, S.M., Chetwynd, J.H., Hoke, M.L., Lockwood, R.B., Gardner, J.A., Cooley,  
1230 T.W., Borel, C.C., & Lewis, P.E. (2005). MODTRAN (TM) 5, a reformulated atmospheric  
1231 band model with auxiliary species and practical multiple scattering options: Update.  
1232 *Algorithms and Technologies for Multispectral, Hyperspectral, and Ultraspectral Imagery*  
1233 *XI, 5806*, 662-667

1234

1235 Calle, A., Casanova, J-L. and Gonzales-Alonso, F. (2009) Impact of point spread function of  
1236 MSG SEVIRI on active fire detections. *International Journal of Remote Sensing*. 30. 17.  
1237 4567-4579.

1238

1239 Center for International Earth Science Information Network (CIESIN) and Centro  
1240 Internacional de Agricultura Tropical (CIAT) Gridded Population of the World Version 3  
1241 (GPWv3). Palisades, NY. CIESIN Columbia University.  
1242 <http://sedac.ciesin.columbia.edu/gpw/index.jsp>.  
1243  
1244 Chen, Y., Li, Q., Randerson, J. T., Lyons, E. A., Kahn, R. A., Nelson, D. L. and Diner, D. J.  
1245 (2009) The sensitivity of CO and aerosol transport to the temporal and vertical distribution of  
1246 North American boreal fire emissions. *Atmospheric Chemistry and Physics*. 9. 6559-6580.  
1247  
1248 Csizar, I., Schroeder, W., Giglio, L., Ellicott, E., Vadrevu, K. P., Justice, C. O. and Wind, B.  
1249 (2014) Active fires from Suomi NPP Visible Infrared Imaging Radiometer Suite : Product  
1250 status and fire evaluation results. *Journal of Geophysical Research : Atmospheres*. 119. 2.  
1251 803-816.  
1252  
1253 DaCamara, C.C. (2006) The Land Surface Analysis SAF: one year of pre-operational  
1254 activity. *The 2006 EUMETSAT Meteorological Satellite Conference*. Helsinki. Finland. 12<sup>th</sup>-  
1255 16<sup>th</sup> June 2006. EUMETSAT P.48, ISBN 92-9110-076-5, 8pp.  
1256  
1257 Derrien, M. and Le Gleau, H. (2005) MSG/SEVIRI cloud mask and type from SAFNWC.  
1258 *International Journal of Remote Sensing*. 26. 21. 4707-4732.  
1259  
1260 EUMETSAT (2007) Active Fire Monitoring with MSG. *Algorithm Theoretical Basis*  
1261 *Document*. EUM/MET/REP/07/0170. Darmstadt. Germany.  
1262  
1263 European Commission (2010) Forest Fires in Europe 2009. EUR 24502 EN. Office for  
1264 Official Publications of the European Communities. Luxembourg. p. 81.  
1265  
1266 Freeborn, P. H., Wooster, M. J., Hao, W. M., Ryan, C. A., Nordgren, B. L, Baker, S. P. and  
1267 Ichoku, C. (2008) Relationships between energy release, fuel mass loss, and trace gas and  
1268 aerosol emissions during laboratory biomass fires. *Journal of Geophysical Research*. 113.  
1269 D01301. doi:10.1029/2007JD008679  
1270

1271 Freeborn, P. H., Wooster, M. J., Roberts, G., Malamud, B. D. and Xu, W. (2009)  
1272 Development of a virtual active fire product for Africa through a synthesis of geostationary  
1273 and polar orbiting satellite data. *Remote Sensing of Environment*. 113. 1700-1711.  
1274

1275 Freeborn, P. H., Wooster, M. J., Roberts, G. (2011) Addressing the spatiotemporal sampling  
1276 design of MODIS to provide estimates of the fire radiative energy emitted from Africa.  
1277 *Remote Sensing of Environment*. 115. 2. 475 – 489  
1278

1279 Freeborn, P. H., Wooster, M. J., Roberts, G. and Xu, W. (2014a) Evaluating the SEVIRI Fire  
1280 Thermal Anomaly Detection Algorithm across the Central African Republic Using the  
1281 MODIS Active Fire Product. *Remote Sensing*. 6. 1890-1917. Doi:10.3390/rs6031890.  
1282

1283 Freeborn, P. H., Cochrane, M. A. and Wooster, M. J. (2014b) A decade long, multi-scale map  
1284 comparison of fire regime parameters derived from three publically available satellite-based  
1285 fire products : a case study in the Central African Republic. *Remote Sensing*. 6. 5. 4061-4089.  
1286

1287 Freeborn, P.H., Wooster, M.J., Roy, D.P., & Cochrane, M.A. (2014c). Quantification of  
1288 MODIS fire radiative power ( FRP) measurement uncertainty for use in satellite- based active  
1289 fire characterization and biomass burning estimation. *Geophysical Research Letters*, 41,  
1290 1988-1994  
1291

1292 Fromm, M., Jerome, A., Hoppel, K., Hornstein, J., Bevilacqua, R., Shettle, E., Servranckx,  
1293 R., Zhanqing, L., and Stocks, B. (2000) Observations of boreal forest fire smoke in the  
1294 stratosphere by POAM III, SAGE II, and lidar in 1998. *Geophysical Research Letters*. 27.  
1295 1407–1410. doi:10.1029/1999GL011200.  
1296

1297 Garcia-Meenedez, F., Hu, Y. and Odman, M. T. (2014) Simulating smoke transport from  
1298 wildland fires with a regional-scale air quality model : Sensitivity to spatiotemporal  
1299 allocation of fire emissions. *Science of the Total Environment*. 493. 544-553.  
1300

1301 Georgiev, C.G., Stoyanova, J.S. (2013) Parallel use of SEVIRI LSA SAF FRP and MPEF  
1302 FIR products for fire detection and monitoring. *2013 EUMETSAT Meteorological Satellite  
1303 Conference. 19<sup>th</sup> American Meteorological Society. AMS Satellite Meteorology,*

1304 *Oceanography and Climatology Conference*. 16<sup>th</sup>-20<sup>th</sup> September. 2013. Vienna. Austria.  
1305 ISSN 1011-3932  
1306  
1307 Giglio, L., Descloitres, J., Justice, C. O., and Kaufman, Y. J., (2003) An enhanced contextual  
1308 fire detection algorithm for MODIS. *Remote Sensing of Environment*. 87. 2-3. 273-282.  
1309  
1310 Gitas, I. Z., Polychronaki, A., Katagis, T and Mallinis, G. (2008) Contribution of remote  
1311 sensing to disaster management activities : A case study of the large fires in the Peloponnese,  
1312 Greece. *International Journal of Remote Sensing*. 29. 6. 1847-1853. Doi:  
1313 10.1080/01431160701874553  
1314  
1315 Govaerts, Y., (2006) RTMOM V0B.10 Evaluation report, report EUM/MET/DOC/06/0502,  
1316 EUMETSAT. 2006. 2226.  
1317  
1318 Govaerts, Y.M., M.Wooster, Freeborn, P., A.Lattanzio and G.Roberts (2010). Algorithm  
1319 Theoretical Basis Document for MSG SEVIRI Fire Radiative Power (FRP) Characterisation.  
1320 EUM/MET/SPE/06/0398. EUMETSAT.  
1321  
1322 Guan, H., Chatfield, R., B., Freitas, S. R., Bergstrom, R. W., Longo, K. M. (2008) Modeling the  
1323 effect of plume-rise on the transport of carbon monoxide over Africa with NCAR CAM.  
1324 *Atmospheric Chemistry and Physics*. 8. 6801–6812.  
1325  
1326 Heil, A., Kaiser, J. W., van der Werf, G. R., Wooster, M. J., Schultz, M. J. and Dernier, van  
1327 der Gron, H. (2010) Assessment of the real-time fire emissions (GFAS) by MACC. Tech  
1328 Memo. 628. *ECMWF*. Reading. UK  
1329  
1330 Holben, B. N., Smirnov, A., Eck, T. F., Slutsker, I., Abuhassan, N., Newcomb, W. W.,  
1331 Schafer, J. S., Tanre, D., Chatenet, B., and Lavenue, F. (2001) An emerging ground-based  
1332 aerosol climatology: Aerosol optical depth from AERONET. *Journal of Geophysical*  
1333 *Research: Atmospheres*. 106. 12 067–12 097. doi: 10.1029/2001JD900014  
1334  
1335 Hollingsworth, A., Engelen, R. J., Benedetti, A., Dethof, A., Flemming, J., Kaiser, J. W.,  
1336 Morcrette, J-J., Simmons, A. J., Textor, C., Boucher, O., Chevallier, F. Rayner, P., Elbern,

1337 H., Eskes, H., Granier, C., Peuch, V-H., Rouil, L., and Schultz, M. G. (2008) Toward a  
1338 Monitoring and Forecasting System For Atmospheric Composition: The GEMS Project.  
1339 *Bulletin of the American Meteorological Society*. 89. 1147–1164. doi:  
1340 <http://dx.doi.org/10.1175/2008BAMS2355.1>  
1341

1342 Ichoku, C. and Kaufman, Y. J. (2005) A method to derive smoke emission rates from MODIS  
1343 fire radiative energy measurements, *IEEE Transactions on Geoscience and Remote Sensing*.  
1344 43. 2636–2649.  
1345

1346 Jacobson, M. Z. (2014) Effects of biomass burning on climate, accounting for heat and  
1347 moisture fluxes, black and brown carbon, and cloud absorption effects. *Journal of*  
1348 *Geophysical Research : Atmospheres*. 119. 8980-9002. Doi:10.1002/2014JD021861.  
1349

1350 Jenkins, B. M., Baxter, L. L., Miles Jr, T. R., and Miles, T. R. (1998) Combustion properties  
1351 of biomass. *Fuel Processing Technology*. 54. 17 – 46.  
1352

1353 Joro, S., Samain, O., Yildirim, A., van de Berg, L. and Lutz, H. J. (2008) Towards an  
1354 improved active fire monitoring product for MSG satellites.  
1355 [www.eumetsat.int/cs/idcplg?IdcService=GET\\_FILE&dDocName=pdf\\_conf\\_p\\_s8\\_47\\_joro\\_v](http://www.eumetsat.int/cs/idcplg?IdcService=GET_FILE&dDocName=pdf_conf_p_s8_47_joro_v&allowInterrupt=1&noSaveAs=1&RevisionSelectionMethod=LatestReleased)  
1356 [&allowInterrupt=1&noSaveAs=1&RevisionSelectionMethod=LatestReleased](http://www.eumetsat.int/cs/idcplg?IdcService=GET_FILE&dDocName=pdf_conf_p_s8_47_joro_v&allowInterrupt=1&noSaveAs=1&RevisionSelectionMethod=LatestReleased)  
1357

1358 Kaiser, J. W., Heil, A., Andrae, M. O., Benedettie, A., Chubarova, N., Jones, L., Morcrette, J-  
1359 J., Razinger, M., Schultz, M. G., Suttie, M. and van der Werf, G., R. (2012) Biomass burning  
1360 emissions estimates with a global fire assimilation system based on observed fire radiative  
1361 power. *Biogeosciences*. 9. 5125-5142. doi:10.5194/bg-9-5125-2012  
1362

1363 Kaiser, J. W., Suttie, M., Flemming, J., Morcrette, J.-J., Boucher, O. and Schultz, M. G.  
1364 (2009a). Global real-time fire emission estimates based on space-borne fire radiative power  
1365 observations. *AIP Conference Proceedings*, 1100:645–648.  
1366

1367 Kaiser, J. W., Boucher, O., Doutriaux-Boucher, M., Flemming, J., Govaerts, Y. M., Gulliver,  
1368 J., Heil, A., Jones, L., Lattanzio, A., Morcrette, J.-J., Perrone, M. R., Razinger, M., Roberts,  
1369 G., Schultz, M. G., Simmons, A. J., Suttie, M., and Wooster, M. J. (2009b). Smoke in the air.  
1370 *ECMWF Newsletter*, 119. 9–15. European Centre for Medium-range Weather Forecasts.

1371

1372 Kaufman, Y. J. and Remer, L. A. (1994) Detection of forests using Mid-IR reflectance : An  
 1373 application for aerosol studies. *IEEE Transactions on Geoscience and Remote Sensing*. 32. 3.  
 1374 672-683.

1375

1376 Koutsias, N., Arianmoutsou, M., Kallimanis, A. S., Mallinis, G., Halley, J. M., and  
 1377 Dimopoulos, P. (2012) Where did the fires burn in Peloponnese, Greece the summer of 2007?  
 1378 Evidence for a synergy of fuel and weather. *Agricultural and Forest Meteorology*. 156. 41-  
 1379 53.

1380

1381 Leung ,F-Y, T., Logan, J. A., Park, R., Hyer, E., Kasischke, E., Streets, S and Yurganov, L.  
 1382 (2007) Impacts of enhanced biomass burning in the boreal forests in 1998 on tropospheric  
 1383 chemistry and the sensitivity of model results to the injection height of emissions. *Journal of*  
 1384 *Geophysical Research*. 112. D10313, doi:10.1029/2006JD008132

1385

1386 Li, Z, Kaufman, Y. J., Ichoku, C., Fraser, R., Trishchenko, A., Giglio, L. and Yu, X. (2001) A  
 1387 review of AVHRR-based active fire detection algorithms: Principles, limitations, and  
 1388 recommendations. *Global and regional vegetation fire monitoring from space, planning and*  
 1389 *coordinated international effort*. Academic Publishing. The Hague. 199-225pp

1390

1391 Liu, Y., Kahn, R. A., Chaloulakou, A. and Koutrakis, P. (2009) Analysis of the impact of the  
 1392 forest fires in August 2007 on air quality of Athens using multi-sensor aerosol remote sensing  
 1393 data, meteorology and surface observations. *Atmospheric Environment*. 43. 3310-3318.

1394

1395 Mallinis, G., Mitsopoulos, I., Stournara, P., Patias, P. and Dimitrakopoulos, A. (2013)  
 1396 Canopy fuel load mapping of Mediterranean pine sites based on individual tree crown  
 1397 delineation. *Remote Sensing*. 5. 6461-6480. Doi:10.3390/rs5126461.

1398

1399 Marlier, M.E., Voulgarakis, A., Shindell, D.T., Faluvegi, G., Henry, C.L. and Randerson, J.T.  
 1400 (2014) The role of temporal evolution in modeling atmospheric emissions from tropical fires.  
 1401 *Atmospheric Environment*. 89. 158-168. doi:10.1016/j.atmosenv.2014.02.039.

1402

1403 MeteoFrance (2010). Algorithm theoretical basis document for cloud products. Technical  
 1404 Report. SAF/NWC/CDOP/MFL/SCI/ATBD/01,MeteoFrance.

1405  
1406 Mistakis, E, Stamos, I., Panakinolaou, A., Aifadopoulou, G. and Kontoes, H (2014)  
1407 Assessment of extreme weather events on transport networks : case study of the 2007  
1408 wildfires in Peloponnesus. *Natural Hazards*. 72. 87-107. Doi:10.1007/s11069-013-0896-3.  
1409  
1410 Mitsopoulos, I. D. and Dimitrakopoulos, A. P. (2013) Estimation of canopy fuel characteristics  
1411 of Aleppo pine (*Pinus halepensis* Mill.) forests in Greece based on common stand parameters.  
1412 *European Journal of Forest Research*. 133:73-79, Doi:10.1007/s10342-013-0740-z.  
1413  
1414 Morcrette, J.-J., L. Jones, J.W. Kaiser, A. Benedetti, O. Boucher (2008) Toward a forecast of  
1415 aerosols with the ECMWF Integrated Forecast System. *ECMWF Newsletter*. No. 114.  
1416 ECMWF. Reading. UK.  
1417  
1418 Paugam, R., Wooster, M., Freitas, S. R. and Val Martin, M. (2015a) A review of approaches  
1419 to estimate wildfire plume injection height within large scale atmospheric chemical transport  
1420 models – Part 1. *Atmospheric Chemistry and Physics Discussions*. 15. 9767-9813.  
1421  
1422 Paugam, R., Wooster, M., Atherton, J., Freitas, S. R., Schultz, M. G. and Kaiser, J. W.  
1423 (2015b) Development and optimization of a wildfire plume rise model based on remote  
1424 sensing data inputs – Part 2. *Atmospheric Chemistry and Physics Discussions*. 15. 9815-9895.  
1425  
1426 Petrenko, M., Kahn, R., Chin, M., Soja, A., Kucsera, T., and Harshvardhan (2012). The use  
1427 of satellite-measured aerosol optical depth to constrain biomass burning emissions source  
1428 strength in the global model GOCART. *Journal of Geophysical Research*. 117(D18):D22204.  
1429 doi:10.1029/2012JD017870  
1430  
1431 Pereira, G., Shimabukuro, Y. E., Moraes, E. C., Freitas, S. R., Cardozo, F., S., and Longo, K.  
1432 M. (2011) Monitoring the transport of biomass burning emission in South America.  
1433 *Atmospheric Pollution Research*. 3. 247-254.  
1434  
1435 Petitcolin, F. and Vermote, E. (2002) Land surface reflectance, emissivity and temperature  
1436 from MODIS middle and thermal infrared data. *Remote Sensing of Environment*. 82. 112-  
1437 134.  
1438

1439 Prins, E. M., and Menzel, W. P., (1994) Trends in South American biomass burning with the  
1440 GOES visible infrared spin scan radiometer atmospheric sounder from 1983 to 1991. *Journal*  
1441 *of Geophysical Research*. 99. 16719-16735.

1442

1443 Prins, E. M., Felts, J. M., Menzel, W. P., Ward, D. E. (1998) An overview of GOES-8 diurnal  
1444 fire and smoke results for SCAR-B and 1995 fire season in South America. *Journal of*  
1445 *Geophysical Research*. 103. 31821-31835.

1446

1447 Poupkou, A., Markakis, K., N.Liora, Giannaros, T. M., Zanis, P., Im, U., Daskalakis, N.,  
1448 Myriokefalitakis, S., Kaiser, J. W., Melas, D., Kanakidou, M., Karacostas, T., and Zerefos, C.  
1449 (2014). A modeling study of the impact of the 2007 Greek forest fires on the gaseous  
1450 pollutant levels in the Eastern Mediterranean. *Atmospheric Environment*. 148. 1–17.

1451

1452 Reid, J. S., Hyer, E. J., Prins, E. M., Westphal, D. L., Zhang, J., Wang, J., Christopher, S. A.,  
1453 Curtis, C. A., Schmidt, C. C., Eleuterio, D. P., Richardson, K. A. and Hoffman, J. P. (2009)  
1454 Global monitoring and forecasting of biomass-burning smoke : description of and lessons  
1455 from the Fire Locating and Modeling of Burning Emissions (FLAMBE) program. *IEEE*  
1456 *Journal of Selected Topics in Applied Earth Observations and Remote Sensing*. 2. 3. 144 -  
1457 162.

1458

1459 Roberts, G., Wooster, M. J., Perry, G. L. W. , Drake, N., Rebelo, L.-M., Dipotso, F. (2005),  
1460 Retrieval of biomass combustion rates and totals from fire radiative power observations:  
1461 Application to southern Africa using geostationary SEVIRI imagery, *Journal of Geophysical*  
1462 *Research*. 110. D21111. doi:10.1029/2005JD006018.

1463

1464 Roberts, G. and Wooster, M. J. (2007) New perspectives on Africa biomass burning  
1465 dynamics. *EOS. Transactions American Geophysical Union*. 88. 38. 369-370.

1466

1467 Roberts, G. and Wooster. M., J. (2008) Fire Detection and Fire Characterization over Africa  
1468 using Meteosat SEVIRI. *IEEE Transactions on Geoscience and Remote Sensing*. 48. 4. 1200-  
1469 1219

1470

1471 Roberts, G and Wooster, M. J. (2014) Development of a multi-temporal Kalman filter  
1472 approach to geostationary active fire detection and fire radiative power (FRP) estimation.  
1473 *Remote Sensing of Environment*. 152. 392-412. DOI: 10.1016/j.rse.2014.06.020  
1474

1475 Roberts, G., Wooster, M. J., and Lagoudakis, E. (2009). Annual and diurnal African biomass  
1476 burning temporal dynamics. *Biogeosciences*, 6, 849-866.  
1477

1478 Roy, D.P. and Boschetti, L. (2009) Southern Africa Validation of the MODIS, L3JRC and  
1479 GLOBCARBON Burned Area Products. *IEEE Transactions on Geoscience and Remote*  
1480 *Sensing*. 47. 4. 1032-1044. doi:10.1109/TGRS.2008.2009000.  
1481

1482 Schroeder, W., Prins, E., Giglio, L., Csiszar, I., Schmidt, C., Morisette, and Morton, D.  
1483 (2008) Validation of GOES and MODIS active fire detection products using ASTER and  
1484 ETM+ data. *Remote Sensing of Environment*. 112. 2711-2726.  
1485

1486 Seiler, W., and Crutzen, P. J. (1980). Estimates of gross and net fluxes of carbon between the  
1487 biosphere and the atmosphere from biomass burning. *Climatic Change*, 2(3), 207-247.  
1488

1489 Sofiev, M., Vankevich, R., Lotjonen, M., Prank, M., Petukhov, V., Ermakova, T., Koskinen,  
1490 J., and Kukkonen, J. (2009) An operational system for the assimilation of the satellite  
1491 information on wild-land fires for needs of air quality modelling and forecasting.  
1492 *Atmospheric Chemistry and Physics*. 9. 6833 – 6847.  
1493

1494 Sofiev, M., Ermakova, T., and Vankevich, R. (2012) Evaluation of the smoke-injection  
1495 height from wild-land fires using remote sensing data. *Atmospheric Chemistry and Physics*.  
1496 12. 1995-2006. doi:10.5194/acp-12-1995-2012.  
1497

1498 Tjemkes, S. A., and Scmetz, J. (1997) Synthetic satellite radiances using the radiance  
1499 sampling method. *Journal of Geophysical Research*. 102. 1807 – 1818  
1500

1501 Theoharatos, G., Pantavou, K., Mavrakis, A., Spanou, A., Katavoutas, G., Efstathiou, P.,  
1502 Mpekas, P., and Asimakopoulos, D (2010) Heat waves observed in 2007 in Athens, Greece:  
1503 Synoptic conditions, bioclimatological assessment, air quality levels and health effects.  
1504 *Environmental Research*. 110. 152–161.

1505

1506 Tsyro, S., Simpson, D., Tarrason, L., Klimont, Z., Kupianen, K., Pio, C. and Yttri, K. E.  
1507 (2007) Modeling of elemental carbon over Europe. *Journal of Geophysical Research :  
1508 Atmospheres*. 112. D23S19. 16. DOI: 10.1029/2006JD008164

1509

1510 Turquety, S., Hurtmans, D., Hadji-Lazaro, J., Coheur, P., Clerbaux, C., Josset, D. and  
1511 Tsamalis, C. (2009) Tracking the emission and transport of pollution from wildfires using the  
1512 IASI CO retrievals: analysis of the summer 2007 Greek fires. *Atmospheric Chemistry  
1513 Physics*. 9. 4897–4913.

1514

1515 Turquety, S., Menut, L., Bessagnet, B., Anav, A., Viovy, N., Maignan, F., & Wooster, M.  
1516 (2014). APIFLAME v1.0: high resolution fire emission model and application to the Euro-  
1517 Mediterranean region. *Geoscientific Model Development*. 7, 587-612, doi:10.5194/gmd-7-  
1518 587-2014.

1519

1520 Val Martin, M., Logan, J. A., Kahn, R. A., Leung, F-Y., Nelson, D. L., and Diner, D. J.  
1521 (2010) Smoke injection heights from fires in North America : analysis of 5 years of satellite  
1522 observations. *Atmospheric Chemistry and Physics*. 10. 1491-1510.

1523

1524 Val Martin, M., Kahn, R. A., Logan, J. A., Paugam, R., Wooster, M. and Ichoku, C. (2012)  
1525 Space-based observational constraints for 1-D fire smoke plume-rise models. *Journal of  
1526 Geophysical Research: Atmospheres*. 117. D22204. Doi: 10.1029/2012JD018370

1527

1528 van der Werf, G. R., Randerson, J. T., Giglio, L., Collatz, G. J., Mu, M., Kasib- hatla, P. S.,  
1529 Morton, D. C., DeFries, R. S., Jin, Y., and van Leeuwen, T. T. (2010). Global fire emissions  
1530 and the contribution of deforestation, savanna, forest, agricultural, and peat fires (1997–  
1531 2009). *Atmospheric Chemistry Physics*. 10. 11707–11735.

1532

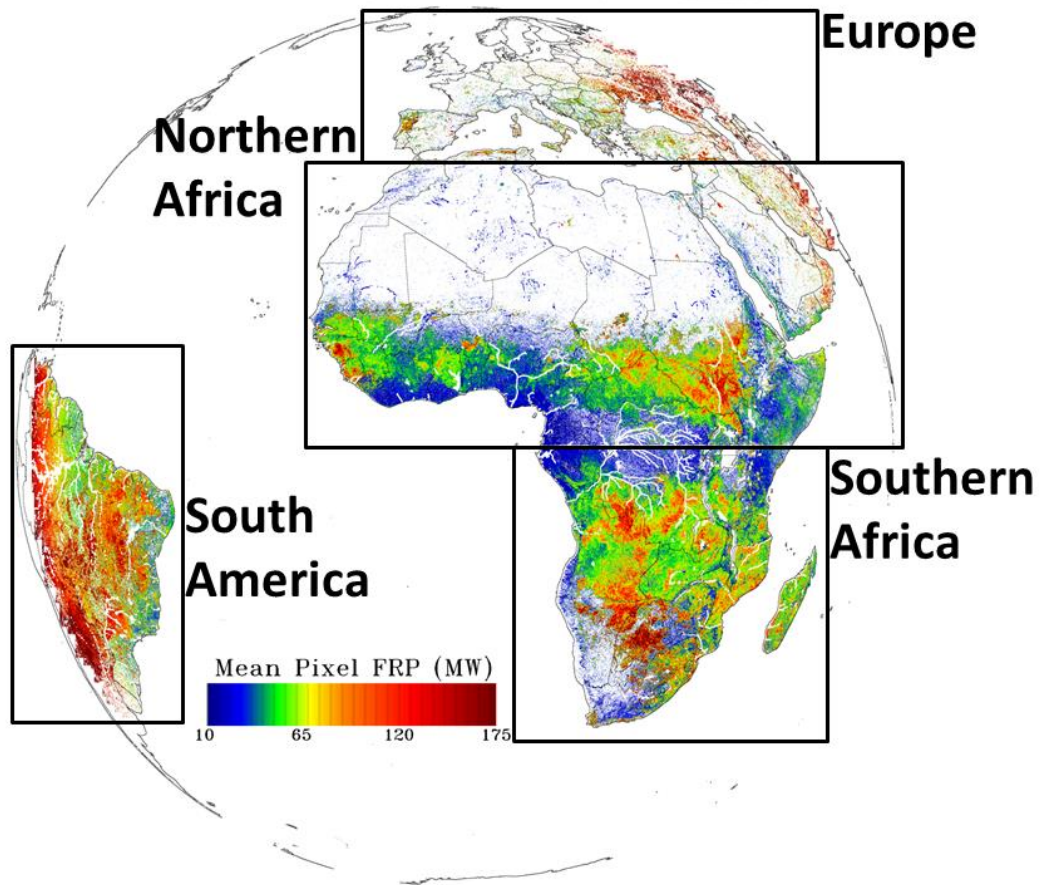
1533 van der Werf, G. R., Randerson, J. T., Giglio, L., Collatz, G. J., Kasibhatla, P. S. and  
1534 Arellano Jr, A. F. (2006) Interannual variability of global biomass burning emissions from  
1535 1997-2004. *Atmospheric Chemistry and Physics*. 6. 3423-3441.

1536

1537 Veraverbeke, S., Lhermitte, S., Verstraeten, W. W. and Goossens, R. (2010) The temporal  
1538 dimension of differenced Normalised Burn Ratio (dNBR) fire/burn severity studies : The case

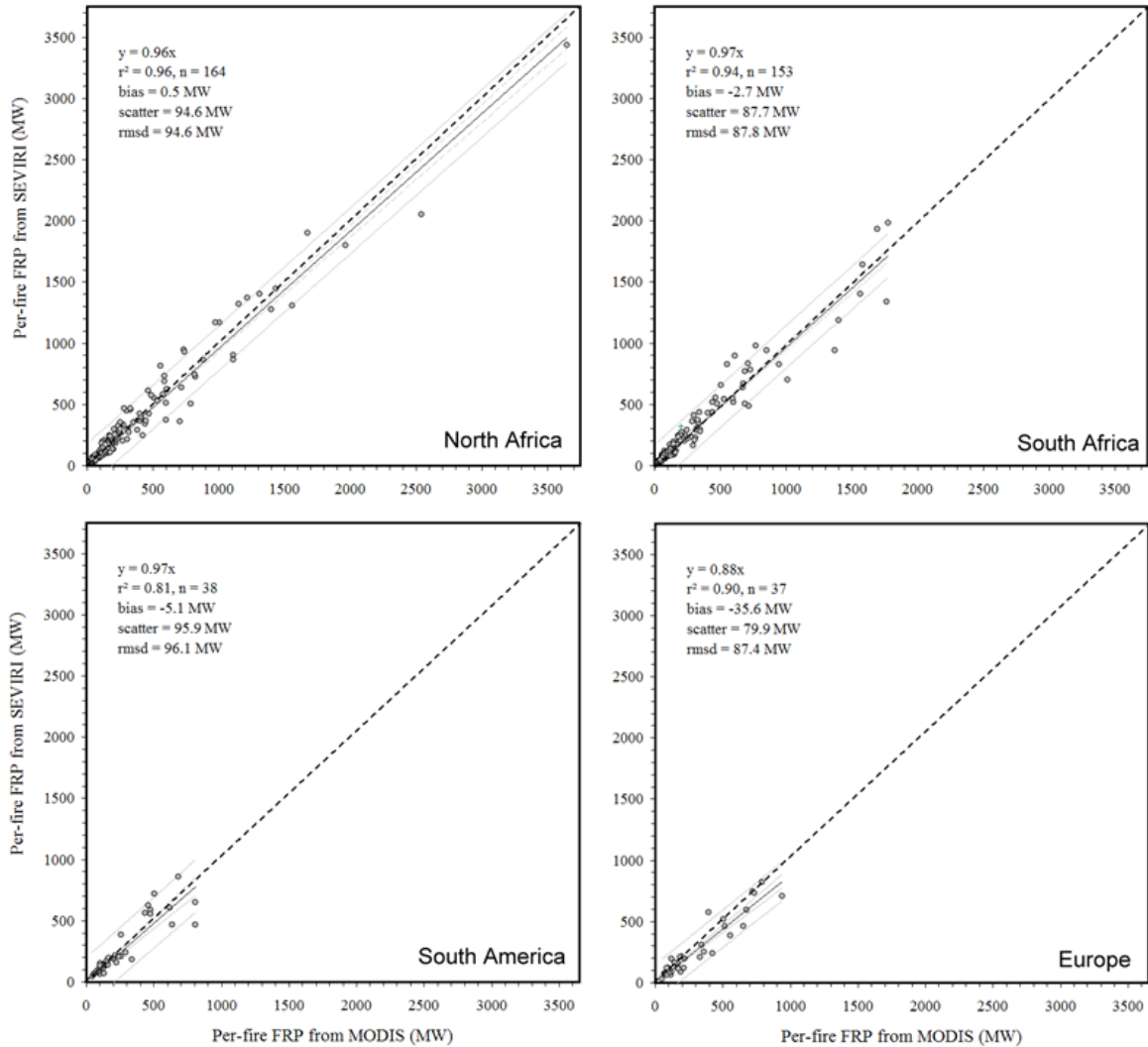
1539 of the large 2007 Peloponnese wildfires in Greece. *Remote Sensing of Environment*. 114. 11.  
1540 2548-2563. Doi: 10.1016/j.rse.2010.05.029  
1541  
1542 Verroios, G and Georgiadis, T. (2011) Aleppo pine forests of northern and western  
1543 Peloponnisos (southern Greece) : Plant communities and diversity. *Plant Biosystems*. 145. 3.  
1544 606-619.  
1545  
1546 World Health Organisation (2006) Air quality guidelines for particulate matter, ozone,  
1547 nitrogen dioxide and sulphur dioxide. WHO/SDE/PHE/OEH/06.02. *World Health*  
1548 *Organization*. WHO Press. Geneva. Switzerland  
1549  
1550 Wooster, M. J., Zhukov, B., and Oertel, D., (2003) Fire radiative energy for quantitative  
1551 study of biomass burning: derivation from the BIRD experimental satellite and comparison to  
1552 MODIS fire products. *Remote Sensing of Environment*. 86. 83-107.  
1553  
1554 Wooster, M. J., Roberts, G., Perry, G. L. W. and Kaufman, Y. J. (2005) Retrieval of biomass  
1555 combustion rates and totals from fire radiative power observations: FRP derivation and  
1556 calibration relationships between biomass consumption and fire radiative energy release.  
1557 *Journal of Geophysical Research*. 110, D24311. doi:10.1029/2005JD006318  
1558  
1559 Wooster, M. J., Xu, W., and Nightingale, T (2012) Sentinel-3 SLSTR active fire detection  
1560 and FRP product: Pre-launch algorithm development and performance evaluation using  
1561 MODIS and ASTER datasets. *Remote Sensing of Environment*. 120. 236–254.  
1562  
1563 Xu, W., Wooster, M. J., Roberts, G. and Freeborn, P. (2010) New GOES imager algorithms  
1564 for cloud and active fire detection and fire radiative power assessment across North, South  
1565 and Central America. *Remote Sensing of Environment*. 114. 9. 1876-1895.  
1566  
1567 Yang, E.-S., Christopher, S. A., Kondragunta, S., and Zhang, X (2011) Use of hourly  
1568 Geostationary Operational Environmental Satellite (GOES) fire emissions in a Community  
1569 Multiscale Air Quality (CMAQ) model for improving surface particulate matter predictions.  
1570 *Journal of Geophysical Research : Atmospheres*. 116. D04303. Doi: 10.1029/2010JD014482.  
1571

1572 Zhang, X., Kondragunta, S., Ram, J., Schmidt, C. and Hung, H-C. (2012) Near-real-time  
1573 global biomass burning emissions product from geostationary satellite constellation. *Journal*  
1574 *of Geophysical Research : Atmospheres*. 117. D14201. doi:10.1029/2012JD017459.  
1575  
1576 Zhukov, B., Lorenz, E., Oertel, D., Wooster, M. and Roberts, G. (2006) Spaceborne detection  
1577 and characterisation of fires during the bi-spectral infrared detection (BIRD) experimental  
1578 small satellite mission (2001-2004). *Remote Sensing of Environment*. 100. 29-51.  
1579 doi:10.1016/j.rse.2005.09.019  
1580  
1581  
1582  
1583  
1584  
1585  
1586  
1587  
1588  
1589  
1590  
1591  
1592  
1593  
1594  
1595



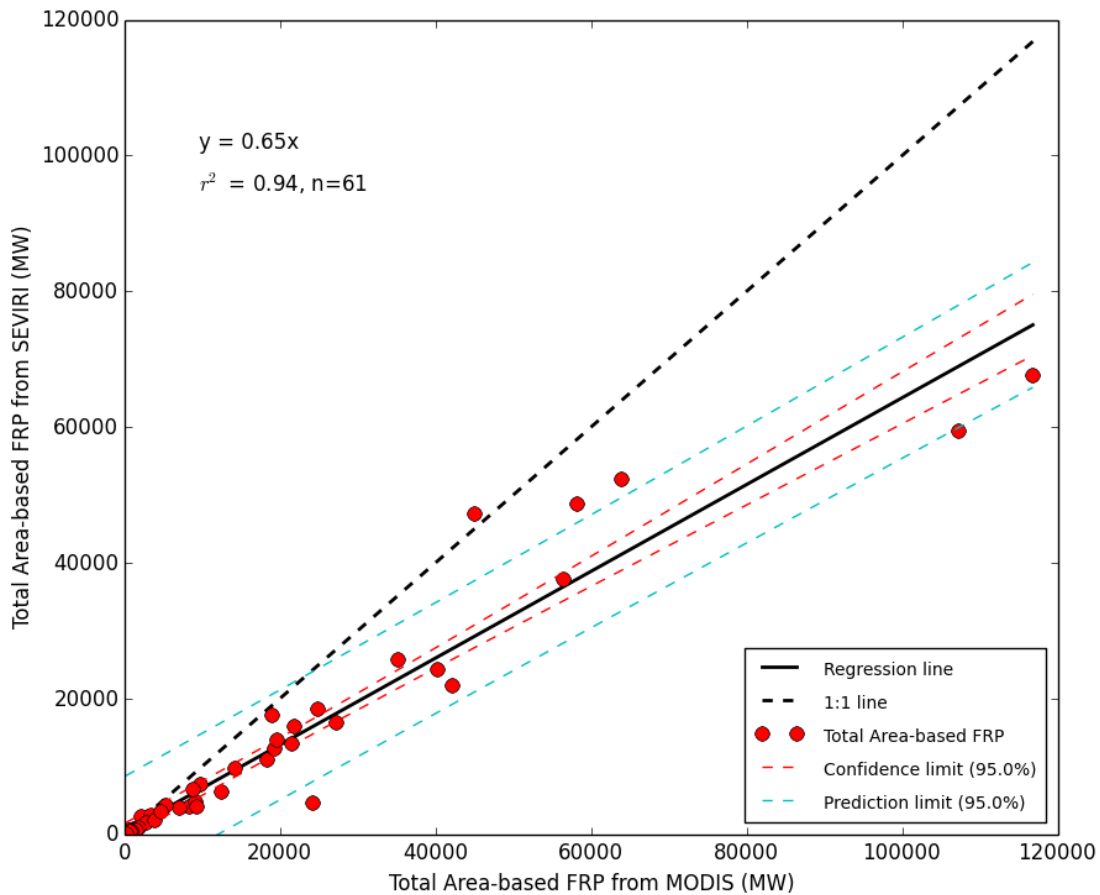
1596  
 1597  
 1598  
 1599  
 1600  
 1601  
 1602  
 1603  
 1604  
 1605  
 1606  
 1607  
 1608  
 1609  
 1610  
 1611  
 1612  
 1613  
 1614  
 1615  
 1616  
 1617  
 1618  
 1619  
 1620

**Figure 1:** SEVIRI's imaging disk showing the mean per-pixel FRP (MW) seen in each SEVIRI pixel, calculated using all FRP-PIXEL products available between 2008-2013. Also indicated are the four geographic regions that LSA-SAF SEVIRI products are subset to.

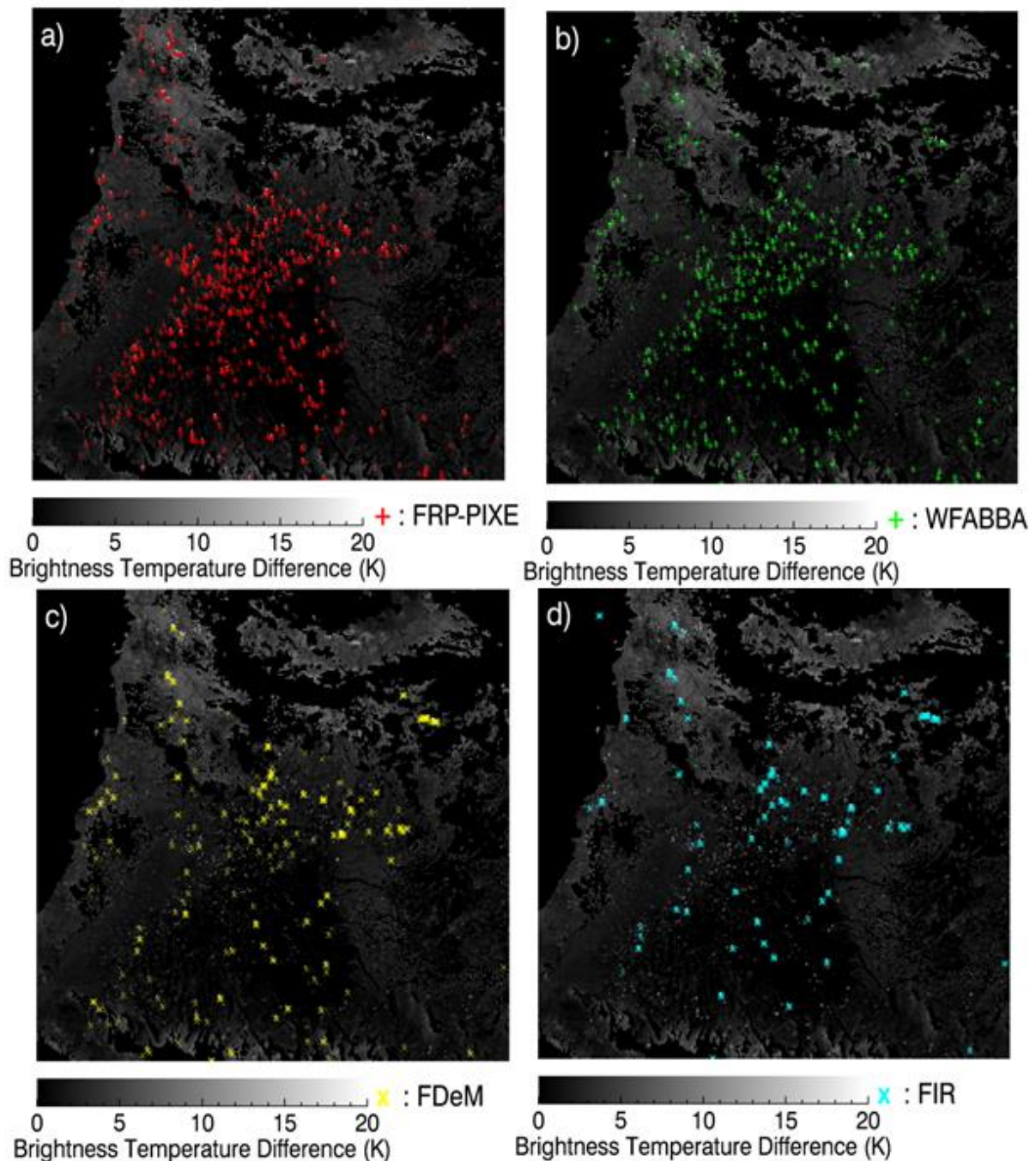


1621  
 1622 **Figure 2:** A comparison of per-fire FRP derived from SEVIRI and MODIS observations of  
 1623 fires observed near-simultaneously by each sensor during one week in each LSA SAF  
 1624 geographic region (Figure 1). Fires are designated as contiguous clusters of active fire pixels.  
 1625 SEVIRI FRP were taken from the LSA SAF FRP-PIXEL product in each case and MODIS  
 1626 FRP is taken from the MOD14 product (Collection 5; Giglio *et al.*, 2003). The most radiant  
 1627 fires were detected in the northern Africa region (top left), and all regions are displayed on  
 1628 the same x- and y-axis scales for ease of comparison.

1629  
 1630  
 1631  
 1632



1633  
 1634 **Figure 3:** Relationship between regional-scale inter-scene FRP derived from all spatially  
 1635 matched, contemporaneous SEVIRI and MODIS FRP-PIXEL observations for the northern  
 1636 Africa region (1-7 December, 2009). The MODIS swath is taken as the observation area. The  
 1637 least squares linear best-fit passing through the origin is shown (bold line), along with the  
 1638 95% confidence intervals on the mean (light dotted line) and on the prediction of y from x  
 1639 (outermost lines). The 1:1 line is also shown (dashed). SEVIRI tends to generally  
 1640 underestimate regional-scale FRP, primarily due to the non-detection of the lowest FRP fire  
 1641 pixels, many of which MODIS can detect. However, the degree of underestimation is  
 1642 relatively small as described by the slope of the linear best fit to the data.  
 1643

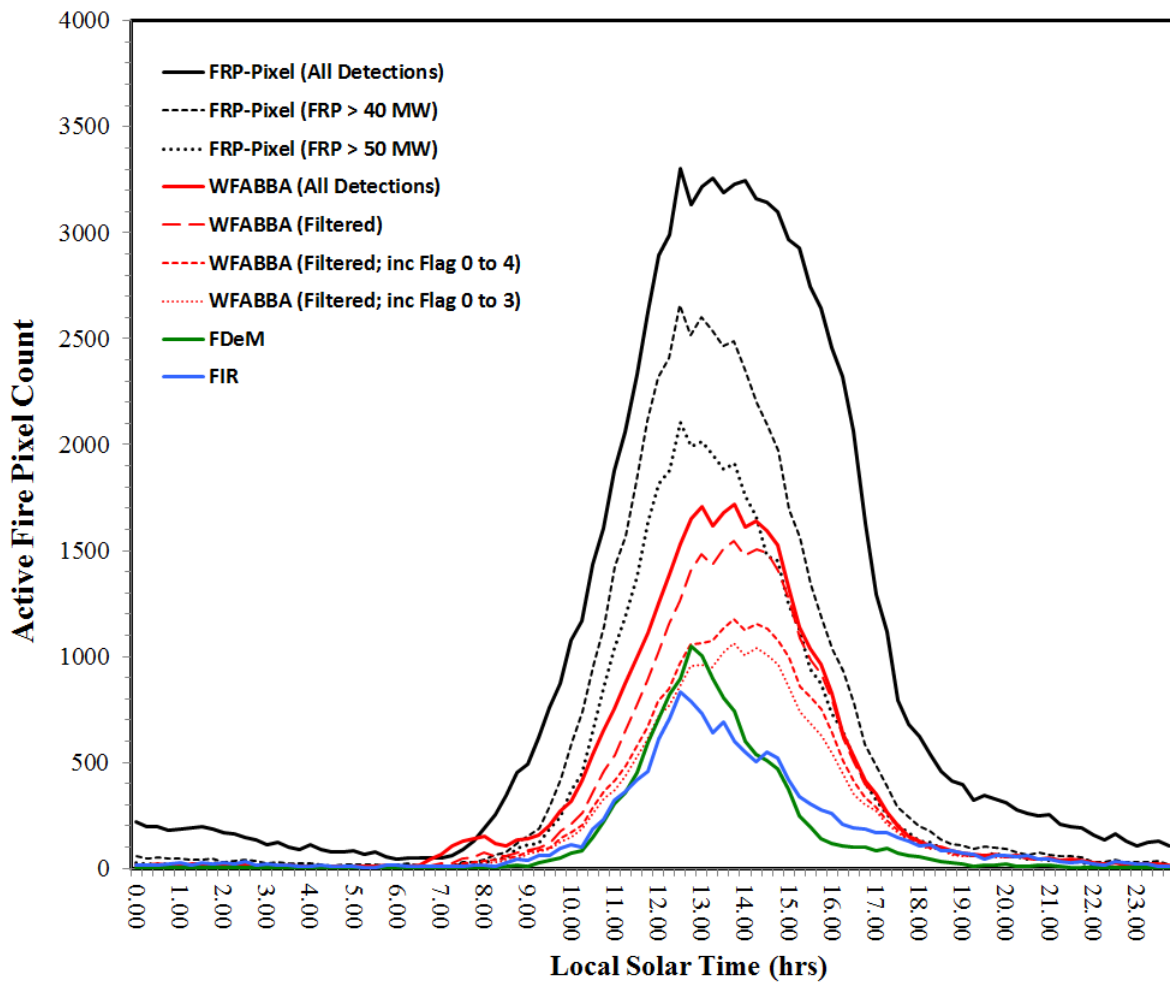


1644  
 1645  
 1646  
 1647  
 1648  
 1649  
 1650  
 1651  
 1652  
 1653  
 1654  
 1655  
 1656  
 1657

**Figure 4** : Example of the active fire pixel detections contained within the four SEVIRI-derived active fire detection products studied herein (LSA SAF FRP-PIXEL product; Wooster *et al.*, 2015, WF-ABBA; Prins *et al.*, 1998, Fire Detection and Monitoring - FDeM; Amraoui *et al.*, 2010, and FIR Active Fire Monitoring; Joro *et al.*, 2008). The images are produced from a single SEVIRI time slot (13:15 UTC on 21<sup>st</sup> August 2014) and show the active fire detections made in (a) FRP-PIXEL (1249 active fire pixel detections), (b) WFABBA (filtered version; 686 detections made), (c) FDeM (346 detections) and (d) FIR (312 detections). The underlying greyscale image is the SEVIRI brightness temperature difference image (3.9 $\mu$ m - 10.8 $\mu$ m channels) from the same imaging slot. Water bodies and clouds have been masked out (black). The region shown is that over Angola in the southern African LSA SAF geographic region (Figure 1). It is clear that whilst all the products tend to detect a reasonable number of fires that are comprised on multiple SEVIRI active fire pixels,

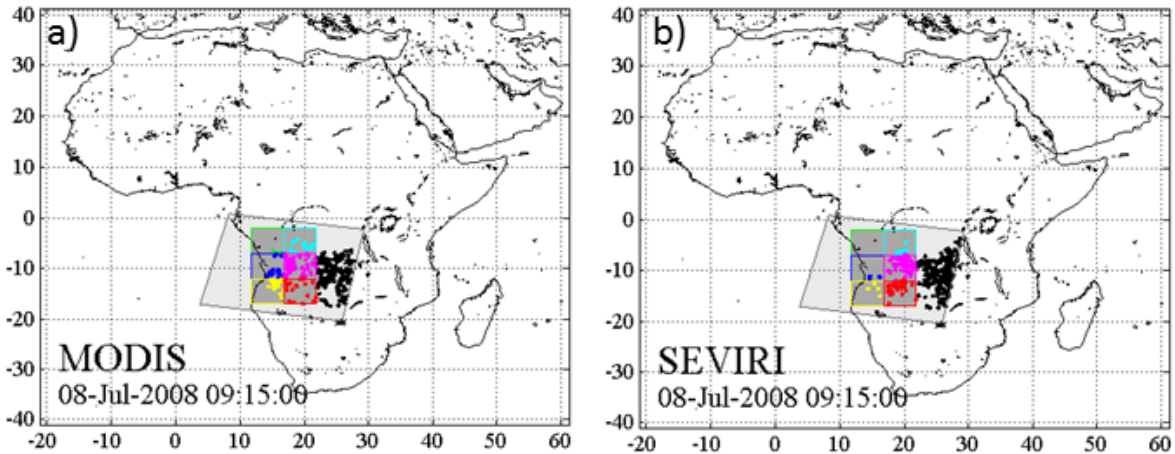
1658 it is the FRP-PIXEL and WF-ABBA products that detect more of the single pixel fires, with  
1659 the FRP-PIXEL product dominating in this regard.  
1660  
1661

1662  
1663



1664  
1665  
1666  
1667  
1668  
1669  
1670  
1671  
1672  
1673  
1674  
1675  
1676  
1677  
1678  
1679  
1680  
1681  
1682  
1683  
1684  
1685

**Figure 5:** Diurnal cycle of active fire detections present within the four SEVIRI-derived active fire products discussed herein for the LSA SAF southern Africa geographic region (Figure 1) on a single day (30<sup>th</sup> August 2014). The products are the LSA SAF FRP-PIXEL product (Wooster *et al.*, 2015), Wildfire-ABBA (WFABBA; Prins *et al.*, 1998), Fire Detection and Monitoring (FDeM; Amraoui *et al.*, 2010) and Active Fire Monitoring (FIR; Joro *et al.*, 2008). All confirmed active fire detections made in each product are included here for completeness, and results are shown in terms of the local solar time of detection. For the FRP-PIXEL product, three active fire time-series are shown; 1) all detections, and those only those detections from fire pixels with FRP magnitudes 2) >40 MW and 3) >50 MW since it is known that increasing undercounting of active fire pixels occurs around these limits (Roberts and Wooster, 2008; and companion paper in this issue). For the WFABBA active fire detections, all four versions of the dataset are included 1) all active fire detections, 2) the WFABBA 'filtered' detections where active fire pixels only detected once during 24 hrs are removed; and the WFABBA filtered detections keeping only 3) the high probability fires (flags 0 to 3) and 4) high and medium probability fires (flags 0 to 4). The LSA SAF FRP-PIXEL product detects a total of 89781 active fire pixels over this day, which reduces to 53561 and 39461 when restricted to fire pixels with FRP >40 MW and >50 MW respectively. For WFABBA, the total number of active fire detections is 35759, and the filtered dataset contains 35759 detections which reduces to 30751 and 23957 when WFABBA low and medium probability fire detections are removed. The FDeM and FIR detect only 13477 and 14645 active fire pixels respectively.



1687

1688

1689

1690

1691

1692

1693

1694

1695

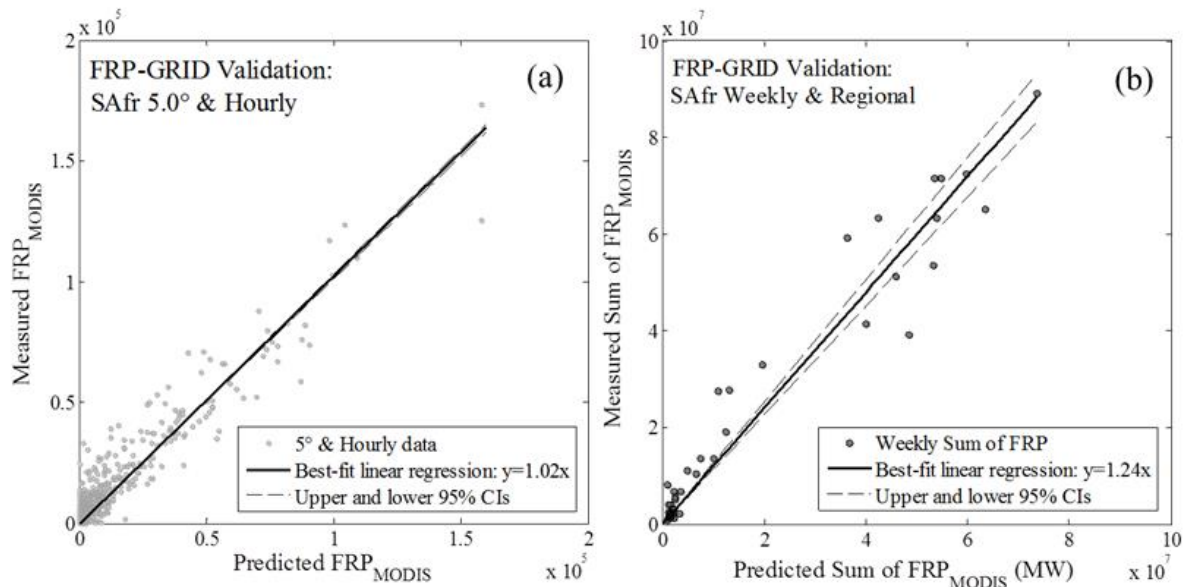
1696

1697

1698

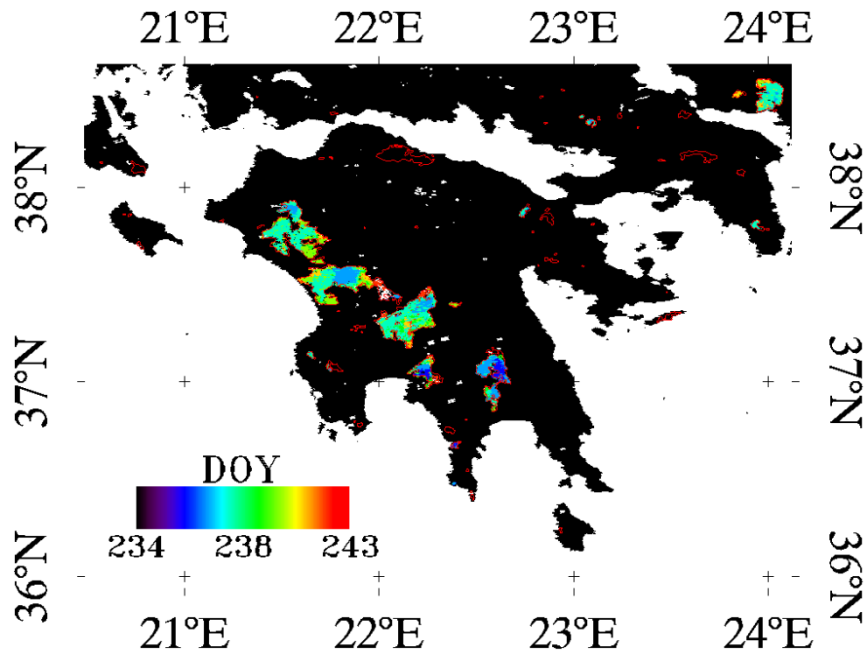
1699

**Figure 6:** Graphical representation of the procedure used to generate the dataset for use in evaluating the bias adjustment factors used within the FRP-GRID product. Fire pixels were subset from the MOD14 and MYD14 MODIS Active Fire products available between May 2008 and April 2009 using six 5.0° grid cells centred on the MODIS swath, as illustrated in (a). These same grid cells were then used in (b) to subset fire pixels from the SEVIRI full Earth disk images acquired at times coincident with the MODIS overpass, as well as from the three previous SEVIRI imaging timeslots collected prior to the MODIS overpass.



1700  
 1701  
 1702  
 1703  
 1704  
 1705  
 1706  
 1707  
 1708  
 1709  
 1710  
 1711  
 1712  
 1713  
 1714  
 1715  
 1716

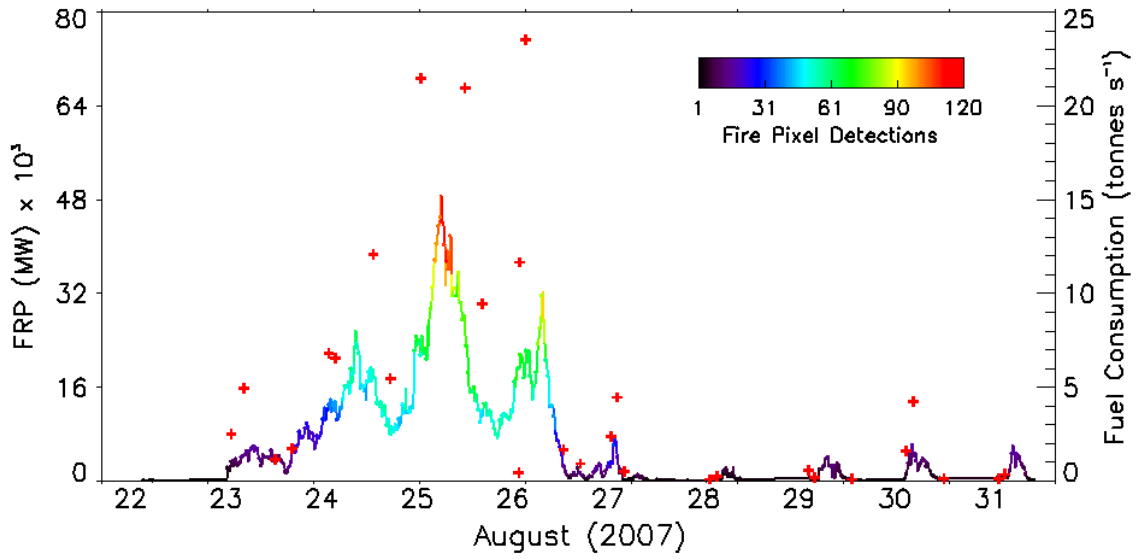
**Figure 7:** Evaluation of the bias adjustment factors used in the SEVIRI FRP-GRID product. Results are based on coincident SEVIRI and MODIS observations taken between May 2008 and May 2009, collected and matched as shown in Figure 6. The nearly 1:1 relationship between the predicted and measured values of MODIS FRP demonstrates the unbiased nature of the adjustment factor applied at (a) 5.0° grid cell resolution and hourly temporal resolution in the FRP-GRID product, in this case for 5.0° grid cells in southern Africa. In (b) the effect of accumulating observations over weekly intervals and over the entire southern Africa LSA SAF geographic region demonstrates that the FRP-GRID product tends to still deliver a result that underestimates the sum of FRP measured by MODIS at this broader spatiotemporal scale, owing primarily to the numerous observations in which SEVIRI failed to detect at least one active fire pixel in a 5.0° grid cell in which MODIS did successfully detect a fire. Full results of the evaluation exercise for all four geographic regions are presented in Table 3.



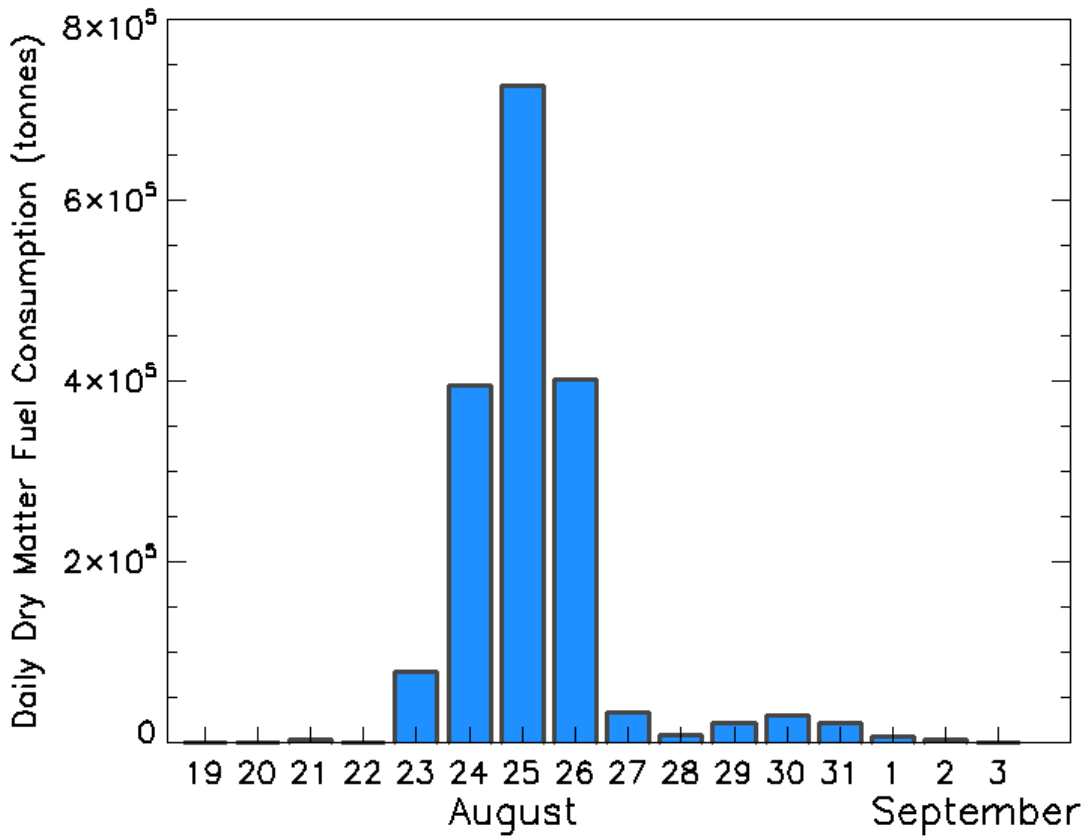
1717 **Figure 8:** The Peloponnese wildfires as viewed by the MODIS 500m burned area of Roy *et*  
 1718 *al.* (2005) collected in August and September 2007 and coloured by day of the year they  
 1719 were detected (DOY). The fires occurred in areas forest, shrublands and olive groves and  
 1720 affected 1847 km<sup>2</sup> according to these data. Also shown as a red outline are the 2007 burned  
 1721 area perimeters extracted from the European Forest Fire Information System (EFFIS;  
 1722 European Commission, 2010) that encompass 1628 km<sup>2</sup>.  
 1723

1724  
 1725  
 1726  
 1727  
 1728  
 1729  
 1730  
 1731  
 1732  
 1733  
 1734  
 1735  
 1736  
 1737  
 1738  
 1739  
 1740  
 1741  
 1742  
 1743  
 1744  
 1745  
 1746  
 1747  
 1748

1749  
1750 a)



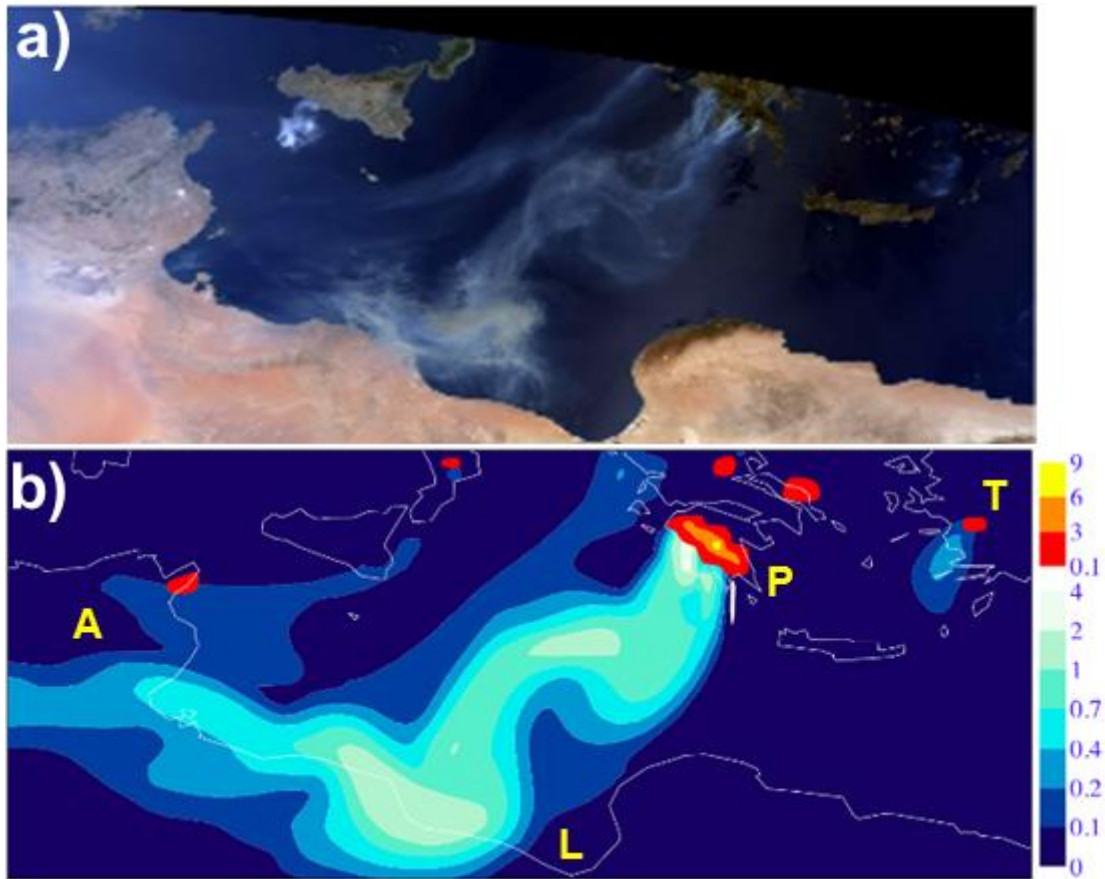
1751  
1752 b)



1753  
1754 **Figure 9:** (a) Time series of atmospherically corrected SEVIRI FRP measures (MW, left  
1755 axis) and equivalent fuel consumption rate (tonnes s<sup>-1</sup>) for the Peloponnese wildfires, as  
1756 measured between 22<sup>nd</sup> and 31<sup>st</sup> August 2007 using the LSA SAF SEVIRI FRP-PIXEL  
1757 product. Also shown are the atmospherically corrected MODIS FRP data collected over the  
1758 same time period (red crosses). Note that for clarity of presentation the MODIS FRP measure  
1759 recorded on 25<sup>th</sup> August (12:05 UTC) is not shown as this exceeds 180 GW, and SEVIRI

1760 reaches a far lower value due to strong prevalence of SEVIRI MWIR channel pixel saturation  
1761 at this time. (b) Daily total dry matter fuel consumption estimated using the time-integrated  
1762 SEVIRI FRP data. We estimate 1.74Tg of fuel was consumed in these fires, the bulk of  
1763 which was burned between 24-26<sup>th</sup> August.  
1764

1765  
1766

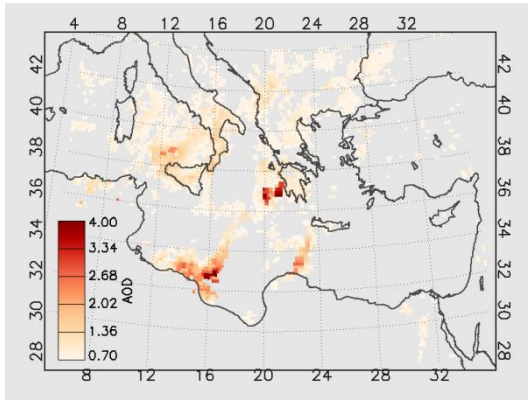


1767  
1768  
1769  
1770  
1771  
1772  
1773  
1774  
1775  
1776  
1777  
1778  
1779  
1780  
1781  
1782  
1783  
1784  
1785  
1786  
1787  
1788  
1789  
1790  
1791

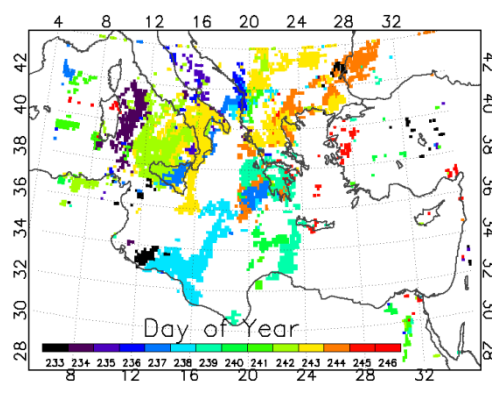
**Figure 10:** (a) MODIS Terra ‘true’ colour composite derived for August 26<sup>th</sup> (09:35 UTC) and (b) fire-emitted smoke aerosol optical depth at 550 nm derived using the modelling scheme detailed in Section 5.2 (blue scale) along with SEVIRI-derived FRP-density observations derived from the FRP-PIXEL product [ $W m^2$ , top, red scale] and interpolated to the atmospheric model grid. The FRP-PIXEL observations indicate the smoke plume sources and highlight the strength of the Peloponnese fires at this time. The Peloponnese (P), Libya (L), Algeria (A) and Turkey (T) are identified. MODIS data source in (a): <http://rapidfire.sci.gsfc.nasa.gov>.

1792  
1793

a)



b)

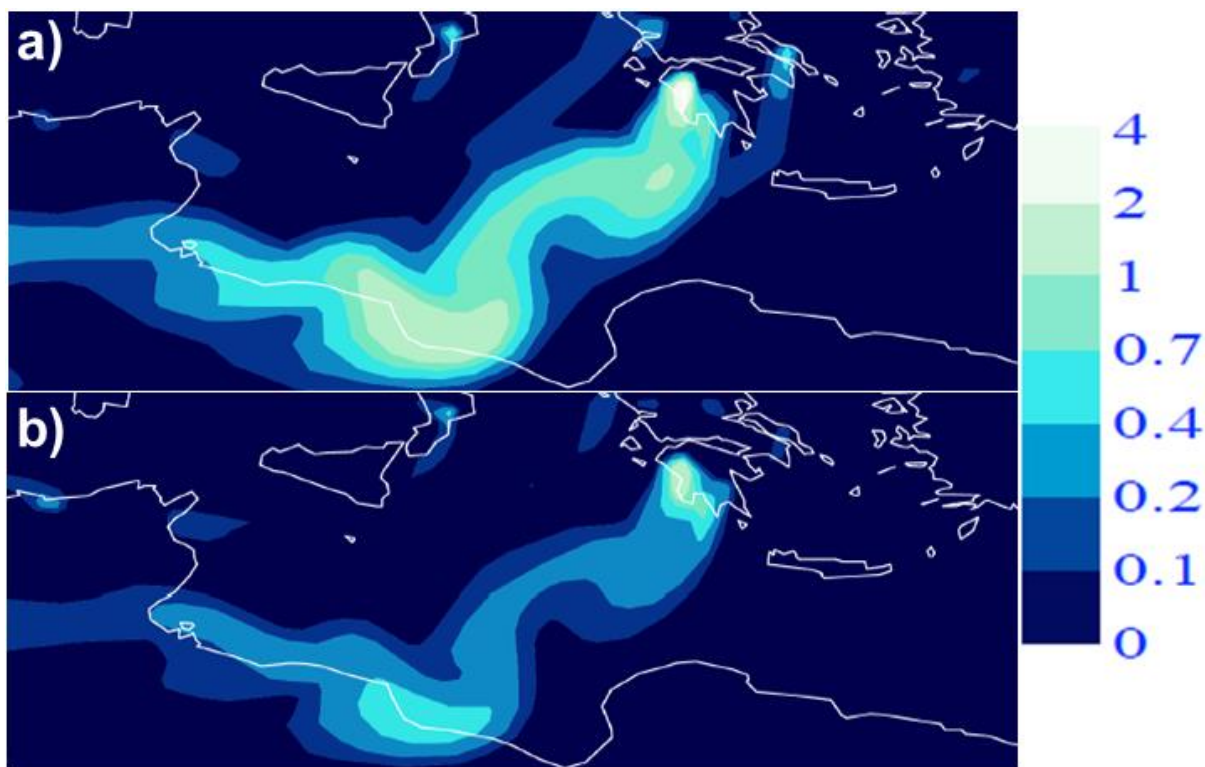


1794  
1795

**Figure 11** : Data extracted for the 2007 Mediterranean 'mega-fire' event from Terra and Aqua MODIS Aerosol Optical Depth (AOD) products (a) Maximum value composite of atmospheric Aerosol Optical Depth (AOD) developed using Terra and Aqua MODIS observations (MOD04 and MYD04 products) acquired between the 21<sup>st</sup> August and 3<sup>rd</sup> September 2007. Only pixels with an AOD value in excess of 0.7 are shown. (b) Day of the year (DOY) of the highest AOD value shown in (a).

1801  
1802  
1803  
1804  
1805  
1806  
1807  
1808  
1809  
1810  
1811  
1812  
1813  
1814  
1815  
1816  
1817  
1818  
1819  
1820  
1821  
1822  
1823  
1824  
1825  
1826  
1827  
1828  
1829  
1830  
1831

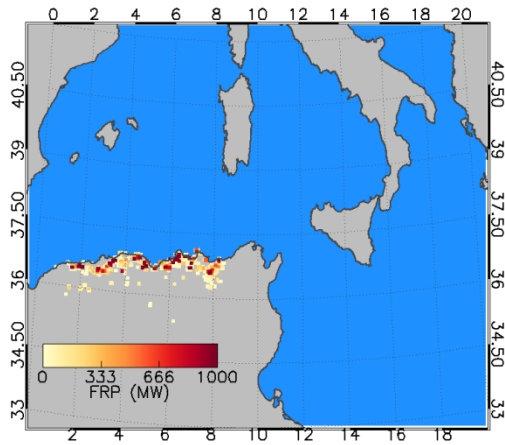
1832  
1833



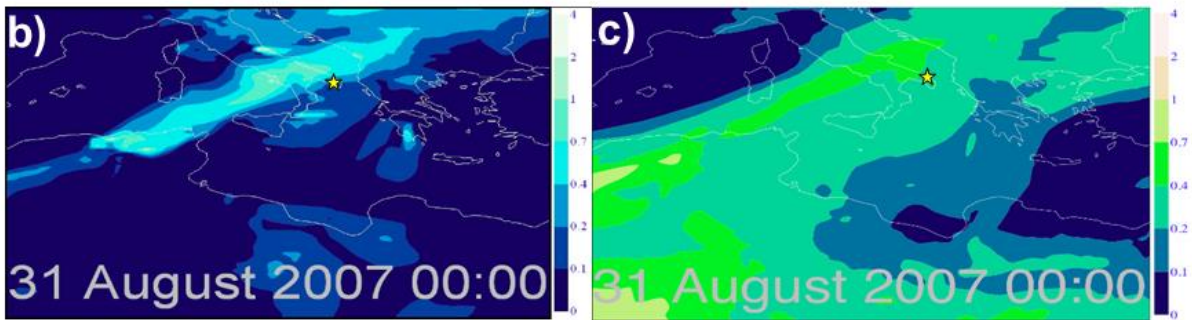
1834  
1835  
1836  
1837  
1838  
1839  
1840  
1841  
1842  
1843  
1844  
1845  
1846  
1847  
1848  
1849  
1850  
1851  
1852  
1853  
1854  
1855  
1856  
1857  
1858  
1859  
1860  
1861

**Figure 12:** Modelled smoke plume on the 26<sup>th</sup> August (09:35 UTC) calculated using (a) daily, and (b) weekly temporal resolution FRP-derived smoke source emissions as described in Section 5.4. The blue scale indicates variations in the modelled smoke aerosol optical depth (AOD) at 550nm. The corresponding modelled AOD obtained using hourly FRP-derived source emissions is shown in Figure 10b.

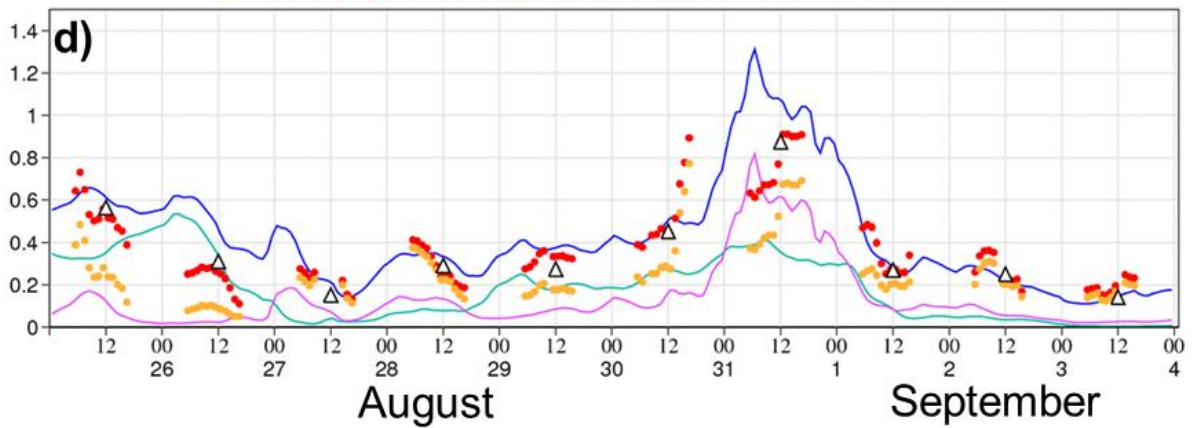
1862 a)



1863



Comparison of model (eyvo) & MODIS AOT at 550nm and L1.5 Aeronet AOT at 500nm  
 FC Total FC Dust FC BC+OM Aeronet Total Aeronet Fine MODIS Total



1864

1865

1866

1867

1868

1869

1870

1871

1872

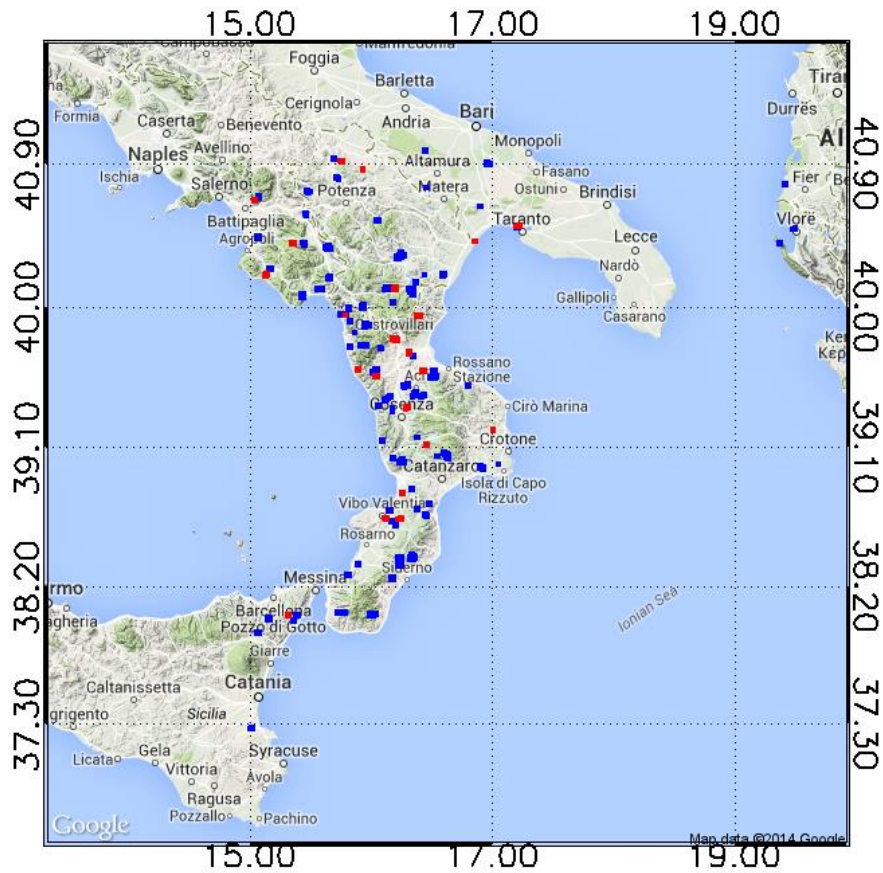
1873

1874

1875

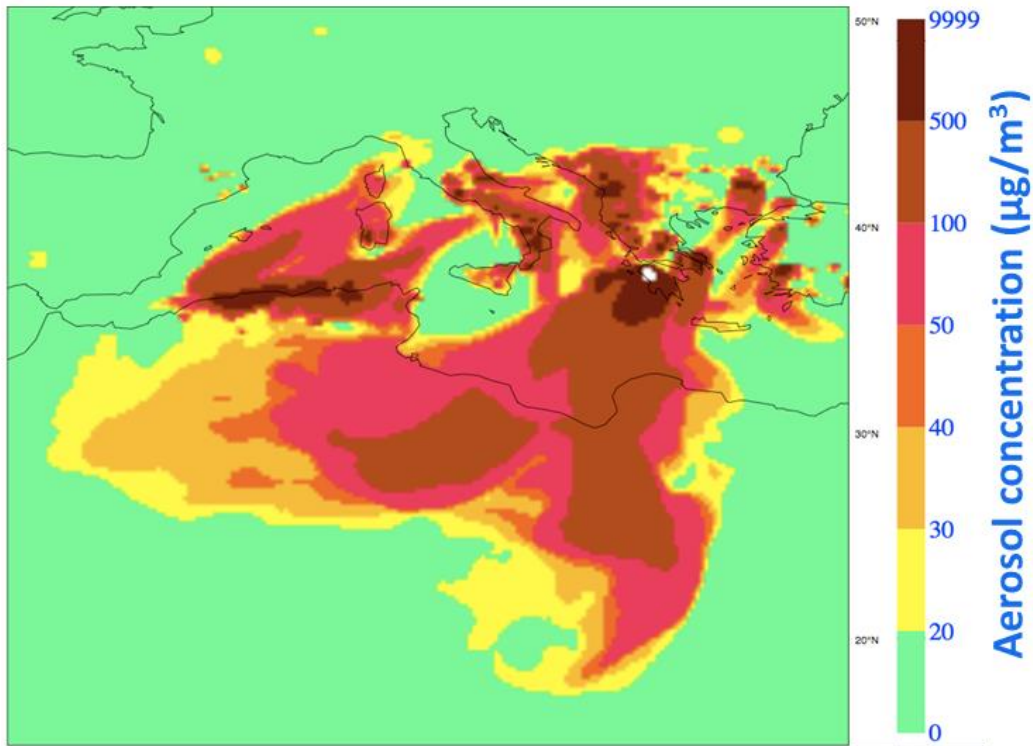
**Figure 13:** MODIS FRP from the Algerian wildfires (a) between the 26<sup>th</sup> August and 4<sup>th</sup> September (2007), (b) modelled smoke, and (c) modelled dust aerosol optical depth (AOD) at 550 nm on August 31<sup>st</sup> 2007 (00:00 UTC). (d) time series of daily averaged MODIS total AOD observations (open black triangles), the AERONET observations of total (red circles) and fine mode AOD (orange circles), modelled total AOD (blue line), and its contributions due to smoke (purple line) and dust (green line). Data sources: MODIS (<http://disc1.sci.gsfc.nasa.gov>) and AERONET (<http://aeronet.gsfc.nasa.gov>)

1876  
1877



1878  
1879  
1880  
1881  
1882  
1883  
1884  
1885  
1886  
1887  
1888  
1889  
1890  
1891  
1892  
1893  
1894  
1895  
1896  
1897  
1898  
1899  
1900  
1901

**Figure 14** : MODIS active fire detections occurring between the 27 and 31<sup>st</sup> August (blue symbols) and 28 and 29<sup>th</sup> August (red symbols). These fires typically occur downwind of the Algerian smoke plume seen in Figure 13, and therefore are likely to have contributed to elevated AOD values detected at the Lecce AERONET site.



1902  
 1903  
 1904  
 1905  
 1906  
 1907  
 1908  
 1909  
 1910  
 1911  
 1912  
 1913  
 1914  
 1915  
 1916  
 1917  
 1918  
 1919  
 1920  
 1921  
 1922  
 1923  
 1924  
 1925  
 1926  
 1927  
 1928  
 1929  
 1930  
 1931

**Figure 15:** Simulated maximum 24-hour running mean smoke aerosol concentration [ $\mu\text{g m}^{-3}$ ] recorded at the surface between the 23<sup>rd</sup> August and 3<sup>rd</sup> September (2007), based on the methodology outlined in Section 5.6. The values are an upper limit due to unrealistically low smoke injection height into the atmosphere. The World Health Organisation (WHO) air quality guidelines (WHO, 2006) set a limit of  $25 \mu\text{g m}^{-3}$  for the surface concentration of fine mode particulate matter (PM<sub>2.5</sub>) averaged over a 24 hour period.

1932 **Table 1:** Performance characteristics of the LSA SAF Meteosat SEVIRI FRP-PIXEL product  
 1933 in the four LSA SAF geographical regions, as compared to MODIS active fire product  
 1934 (Collection 5 MOD14 and MYD14) collected over the same area and at the same time. Errors  
 1935 of omission and commission with respect to MODIS were calculated on a per fire pixel basis  
 1936 as described in Section 3.1.1. The per-fire basis results (Column 5) were obtained when  
 1937 comparing the total FRP retrieved from MODIS and SEVIRI for fires (defined as a spatially  
 1938 contiguous set of active fire pixels) detected by both sensors. The area-based results (column  
 1939 6) were derived from comparison of the total FRP measured by all detected fires in a  
 1940 matching MODIS and SEVIRI image area, and thus include the influence of non-detected  
 1941 low FRP fires by SEVIRI whilst the per-fire comparison results (Column 5) do not.

1942

<b>LSA SAF Geographic Region</b>	<b>Image Dates (2008)</b>	<b>Active Fire Pixel Detection Omission Error (%)</b>	<b>Active Fire Pixel Detection Commission Error (%)</b>	<b>Slope of linear best fit relationship between SEVIRI-to-MODIS per-fire-based FRP measures</b>	<b>Slope of linear best fit relationship between SEVIRI-to-MODIS Area-based FRP measures</b>
northern Africa	1-8 Dec	65	9	0.96	0.65
southern Africa	19-24 Aug	77	13	0.97	0.53
South America	14-24 Aug	91	39	0.97	0.22
Europe	9-17 Aug	97	30	0.88	0.11

1943  
 1944  
 1945  
 1946  
 1947  
 1948  
 1949  
 1950  
 1951  
 1952  
 1953  
 1954  
 1955  
 1956  
 1957  
 1958  
 1959  
 1960  
 1961  
 1962

1963  
1964  
1965  
1966  
1967  
1968  
1969  
1970  
1971

**Table 2** : Summary of active fire pixel detection errors of omission and commission for the four SEVIRI-derived active fire products explored herein (LSA SAF FRP-PIXEL product; Wooster *et al.*, 2015, WF-ABBA; Prins *et al.*, 1998, Fire Detection and Monitoring - FDeM; Amraoui *et al.*, 2010, and FIR Active Fire Monitoring; Joro *et al.*, 2008). Data were collected over the LSA SAF southern Africa geographic region during August 2014, when fire activity is widespread in this area. The MODIS active fire products (MOD14 and MYD14; Giglio *et al.*, 2003) acted as the independent data source for the comparison.

	<b>FRP-PIXEL</b>	<b>WFABBA</b>	<b>WFABBA</b>	<b>WFABBA</b>	<b>WFABBA</b>	<b>FDeM</b>	<b>FIR</b>
		<b>All Detection s</b>	<b>Filtered</b>	<b>Filtered (Flags 0-4)</b>	<b>Filtered (Flags 0-3)</b>		
Number of SEVIRI fire pixels at coincident MODIS overpasses	33414	15610	13008	9736	8832	7664	7151
Number of SEVIRI fire pixels detected by MODIS	29037	14521	12284	9369	8496	7260	6730
Commission error (%)	13	7	6	4	4	5	6
Omission error (%)	77	82	84	87	88	92	95

1972  
1973  
1974  
1975  
1976  
1977  
1978  
1979  
1980  
1981  
1982  
1983  
1984  
1985  
1986  
1987  
1988  
1989  
1990  
1991  
1992

1993  
 1994  
 1995  
 1996  
 1997  
 1998  
 1999  
 2000  
 2001

**Table 3:** Summary of the results related to evaluation of the regional bias adjustment factors implemented during the processing of the LSA SAF FRP-GRID product. Slope of the linear best fit between the SEVIRI-predicted regional FRP using the FRP-GRID bias adjustment factors and the FRP measured by MODIS over the same areas are shown, as are the coefficients of determination ( $r^2$ ), at both  $5^\circ$  and hourly resolution (which is the native FRP-GRID product resolution) and also at a weekly resolution accumulated over the entire LSA SAF geographic region.

LSA SAF Region	Abbreviation	Validation Results: Slope ( $r^2$ )	
		$5.0^\circ$ and hourly	weekly and regional
northern Africa	NAfr	1.04 (0.76)	1.15 (0.96)
southern Africa	SAfr	1.02 (0.91)	1.24 (0.97)
South America	SAMe	0.97 (0.34)	1.89 (0.83)
Europe	Euro	1.72 (0.19)	4.94 (0.84)

2002  
 2003  
 2004  
 2005  
 2006  
 2007  
 2008  
 2009  
 2010  
 2011  
 2012  
 2013  
 2014  
 2015  
 2016  
 2017  
 2018  
 2019  
 2020  
 2021  
 2022  
 2023  
 2024  
 2025  
 2026  
 2027  
 2028  
 2029  
 2030  
 2031  
 2032  
 2033  
 2034  
 2035  
 2036

2037  
2038  
2039  
2040  
2041  
  
2042  
2043  
2044  
2045  
2046  
2047  
2048  
2049  
2050  
2051  
2052  
2053  
2054  
2055  
2056  
2057  
2058  
2059

**Table 4:** Trace gas and particulate smoke emission factors ( $\eta$ ) for species (*s*) based on extratropical forest fuels, taken from Andreae and Merlet (2001). \* The emission factor for BC and OC was derived specifically for use in this study (see main text).

<b>Species</b>	<b>Emissions factor (g kg<sup>-1</sup> DM)</b>
Black carbon (BC)	1.7*
Organic carbon (OC)	8.6-9.7
Organic matter (OM)	42*
Total particulate matter (TPM)	17.6±6.4
Fine mode aerosol (PM2.5)	13.0±7.0
Carbon Monoxide (CO)	107±37